A First Assessment of Adjoint Body-Force Modeling Capabilities for Fan Design

Cyril Dosne, Raphaël Barrier, Marco Carini, Rocco Moretti, Sébastien Bourasseau, Jacques Peter

A First Assessment of Adjoint Body-Force Modeling Capabilities for Fan Design

Cyril Dosne * and Raphaël Barrier[†], Marco Carini[‡], Rocco Moretti[§]
DAAA, ONERA, Université de Paris Saclay, F-92190 Meudon - France

Sébastien Bourasseau[¶], Jacques Peter[‖]
DAAA, ONERA, Université de Paris Saclay, F-92322 Châtillon - France

Body-Force Modeling methods have proven their capacity to faithfully reproduce both the engine performance trends and the distortion transfer across the successive blade rows under inlet distortions. Their CPU and memory costs are significantly lower than those of blade-resolved simulations, like unsteady RANS. Therefore, they are of high interest for studying disruptive engine systems, such as distributed propulsion, boundary-layer ingestion systems or unducted fans. These systems exhibit strong coupling between the airframe and the engine, resulting in engine inlet distortions. The Hall body-force model presents a direct dependency to the fan blade shape parameters, with no mandatory prerequisite calibration, making it suitable for gradient-based optimizations. However, body-force models lack an adjoint formulation to be efficiently used in gradient-based optimizations involving a large number of design variables at once. In this context, a discrete adjoint formulation based on explicit body-force modeling is proposed to tackle fan shape optimizations for preliminary design stage. This will allow us to perform a first assessment of the adjoint body-force design capabilities under inlet distortions. It will also pave the way for using the adjoint body-force to conduct highly coupled aero-propulsive optimizations of both the airframe and the engine geometries simultaneously. First, the explicit body-force modeling methodology and its adjoint specificities are detailed. Second, the validation of the Hall adjoint formulation is undertaken on a simple fan-stator configuration. Then, adjoint gradients provided by the body-force methodology are compared to their blade-resolved counterpart - i.e. classical RANS simulations with discretized blade geometries - to assess the reliability of the Hall model to conduct fan shape designs, for various operating conditions. Finally, the next steps required before performing a simultaneous optimization of both the airframe and the engine geometries are discussed.

I. Nomenclature

ABFM	=	Adjoint Body-Force Modeling
BFM	=	Body-Force Modeling
BLI	=	Boundary-Layer Ingestion
CFD	=	Computational Fluid Dynamics
CPU	=	Central Processing Unit
HNL	=	Hall No Losses, i.e. only the normal force of the Hall model
QNC	=	Quadratic Not Calibrated, i.e. the normal force of the Hall model with not calibrated quadratic losses
QoI	=	Quantity of Interest
RANS	=	Reynolds Averaged Navier Stokes
URANS	=	Unsteady Reynolds Average Navier Stokes
β	=	engine design parameters

*Ph.D. Student, Aerodynamics, Aeroelasticity and Acoustics Dept, cyril.dosne@onera.fr
[†]Dr. Research engineer, Aerodynamics, Aeroelasticity and Acoustics Dept, raphael.barrier@onera.fr
[‡]Dr. Research engineer, Aerodynamics, Aeroelasticity and Acoustics Dept, marco.carini@onera.fr
[§]Dr. Research engineer, Aerodynamics, Aeroelasticity and Acoustics Dept, rocco.moretti@onera.fr
[¶]Dr. Computer engineer, Aerodynamics, Aeroelasticity and Acoustics Dept, sebastien.bourasseau@onera.fr
[‖]HDR. Research Scientist, Aerodynamics, Aeroelasticity and Acoustics Dept

$\beta^{\#}_{X_{BFM}}$	=	body-force discrete input fields of the *BACARDI* module
$\beta^{row}_{hX\ mY}$	=	camber control point, placed on the skeleton of the row row, at the relative channel height X% and the relative chord position Y%
Π	=	compressor stage compression ratio
η	=	compressor stage isentropic efficiency
$\tilde{\mathbf{\Lambda}}$	=	adjoint vector, solution of the adjoint body-force equations
Ω	=	row rotation speed, as input of the *BACARDI* module
$\overrightarrow{f}$	=	modeled blade force
f_n	=	normal component of the modeled blade force
f_p	=	parallel component of the modeled blade force
h	=	relative channel height
$\mathcal{J}$	=	QoI of the optimization problem, function of the discretized mesh, the flow, and the source term variables
m	=	relative chord position
$\dot{m}$	=	full-annulus mass flow rate
$\dot{m}_{BLO}$	=	operating point near the blockage
$\dot{m}_{ME}$	=	operating point within the designed operating range of the compressor
$\dot{m}_{SL}$	=	operating point near the compressor stability limit
N	=	row blades number, as input of the *BACARDI* module
n_x	=	axial component field of the normal to the blade skeleton, as input of the *BACARDI* module
n_θ	=	azimuthal component field of the normal to the blade skeleton, as input of the *BACARDI* module
n_r	=	radial component field of the normal to the blade skeleton, as input of the *BACARDI* module
P_{out}	=	outlet static pressure
Q_{POW}	=	power delivered by the fan to the flow
$\boldsymbol{R}$	=	discretized RANS residual vector
$\tilde{\boldsymbol{R}}$	=	augmented RANS residual vector, integrating the source term forcing
$\boldsymbol{S}$	=	discretized body-force source terms
$\boldsymbol{S}_\rho$	=	discretized body-force density source term field
$\overrightarrow{\boldsymbol{S}_{\rho v}}$	=	discretized body-force momentum source term fields
$\boldsymbol{S}_{\rho E}$	=	discretized body-force energy source term field
$\boldsymbol{S}_{\tilde{\nu}}$	=	body-force turbulence source terms
$\boldsymbol{W}$	=	CFD flow solution
$\boldsymbol{X}$	=	CFD mesh
$\boldsymbol{X}_{BFM}$	=	body-force "blade-fitted" mesh, generated from its blade-resolved counterpart

II. Introduction

Between 1973 and 2018, aviation CO_2 emissions have increased by 176%, while the energy consumption per passenger-kilometer has been reduced by 79% [1]. Further aircraft efficiency gains are required to meet the 50% drop of air traffic carbon footprint by 2050 relative to 2005 levels [2]. Over the past decades, conventional aircraft configurations have been optimized while minimizing the aerodynamic interactions between the airframe and the engines, integrating them under the wings or mounted on the fuselage side. However, further increase of the engine bypass ratio would lead to strong aerodynamic interaction between the airframe and the fan at some operating points [3, 4]. Besides, new engine integration architectures have been proposed to exploit aero-propulsive synergies. They consist for instance of propulsive systems distributed over the airframe or turbofans engines ingesting the fuselage boundary-layer (BLI designs). Such design leads to strong inlet distortions at the engine face, which may strongly alter its performance and its operability limits [5–7]. Therefore, it is essential to undertake turbofan design under inlet distortions starting from the early design phases.

In the past years, such analyses have been conducted, using propulsion models to ensure a reasonable computational cost of the studies. Indeed, even when considering a stationary azimuthal inlet distortion in the aircraft reference frame, the blade perceives a periodic forcing, which can lead to unsteady phenomena. To assess their effect on the propulsive efficiency, conventional methods modeling the blade movement would require an unsteady approach to analyze the distortion transfer across the engine [3, 4, 8]. Since classical high-fidelity simulations as URANS are cost prohibitive for

preliminary optimization studies, propulsive models are needed. Aero-propulsive optimizations have been undertaken in the literature to minimize the inlet distortion at the engine face [9, 10] or the power consumption [11] for BLI configurations. They all used boundary conditions at the inlet and outlet fan-swept volume surfaces, meaning neither the distortion transfer across the engine nor the swirl jump across the fan could be captured. Ordaz *et* al [12] used an Actuator Disk modeling combined with Blade Element Theory computations to enhance the engine modeling. They were able to capture the swirl jump across the propeller plane, but such a method cannot capture the distortion transfer across the blade row since the methodology is purely bi-dimensional. Other studies have shown that the fan aerodynamic response to inlet distortion leads to upstream total pressure and flow velocity redistribution, and is therefore key to capture the distortion pattern itself [4, 13]. Therefore, it appears essential to model the distortion transfer across the engine, and to capture the blade aerodynamic response to this distortion, to correctly evaluate the engine performance. Similarly, it is also crucial in order to study the aero-propulsive coupling effects between the airframe and the propulsive subsystem. In this spirit, Gray *et* al [14] enhanced their engine model to modulate the fan thrust considering the engine inlet flow state, and thus inlet distortions, and to simulate the flow transfer across the engine through a body-force alike method. Latter, they demonstrated the capabilities of this engine model to conduct turbofan pre-design using the adjoint method [15, 16]. However, this model cannot fully reproduce the distortion transfer across the engine, nor the swirl jump across the fan row.

Engine models of higher fidelity, like explicit body-force models, have been used to study the aero-propulsive coupling phenomena and the influence of inlet distortions on the fan performance. Vega, Dufour and García Rosa [7] used an explicit body-force model on a turbofan secondary airflow to estimate the full engine performance under a BLI alike inlet distortion, showing a small drop of power consumption despite the penalties observed on the fan and the thermal efficiencies and the reduction of the surge margin. Body-force models have indeed proven capable of correctly assessing the engine propulsive efficiency under distorted conditions and faithfully reproducing the distortion transfer across the engine stages [6]. They can capture the main aero-propulsive coupling effects, including distortions [3, 17, 18] at a computational cost two orders of magnitude lower than the URANS [6]. Explicit body-force models rely on an analytical formulation of the body force $\overrightarrow{f}$ as a function of the mesh, the flow and the engine variables. Some of them have a direct dependence on blade shape parameters, like the local camber or chord. For instance, the Hall model [5], improved by Thollet [8], introduces a direct dependence on blade shape parameters and do not necessarily prerequisites high-fidelity computations, making it suitable for optimization studies handling airframe and engine blade parameters at once. Parametric studies on fan-nacelle coupling and enhanced designs [3, 4], and then first rotor and stator blade shape optimizations under inlet distortions [5, 6] using body-force explicit models have shown interesting results. Recently, this model has been extended to the performance and flow analysis of propeller blades [19]. However, to the best of the authors' knowledge, no adjoint formulation of these models has been proposed so far in the literature, nor a precise evaluation of the Body-Force Modeling (BFM) capabilities for fans shape design. The lack of an efficient method to compute the gradients of the Quantities of Interest (QoI) with respect to the design parameters restricts the design space dimension that can be explored during the optimization at an affordable computational cost. It also implies robustness issues in the optimization loop when using finite differences [6]. To efficiently integrate the BFM in a gradient-based optimization framework, the need for an adjoint body-force formulation appears. Attempts were undertaken at TU Delft in that direction, through various master thesis projects, but provided mixed results [20, 21].

In this context, the goal of this paper is to introduce a 3D discrete adjoint formulation of the Hall model in the framework of the elsA CFD solver [22, 23], using source-transformation algorithmic differentiation tools [24], and to precisely evaluate its design capability for various operating conditions and various blade shape parameters. First, a short reminder of the body-force methodology is presented, focusing on the BFM models investigated in this paper. Then, the mathematical formulation of the adjoint body-force is described, and the validation of the adjoint body-force gradients are undertaken. Then, a first evaluation of the Hall model design capability using the Adjoint Body-Force Modeling (ABFM) is performed on a compressor test case. Finally, the on-going developments and analysis towards coupled aero-propulsive simultaneous optimizations are discussed.

III. Body-Force modeling and Adjoint body-force equations

All BFM methods rely on simulating the blade effect on the engine flow by adding source terms to the right-hand side of the RANS equations. The general formulation is summarized in eq. (1). We denote by $\boldsymbol{X}$ the CFD mesh, $\boldsymbol{W}$ the corresponding flow solution, $\boldsymbol{S}$ the body-force source terms, $\boldsymbol{R}$ the residual vector of the discretized RANS equations

and $\tilde{\boldsymbol{R}}$ its augmented form including body-force source terms:

$$\boldsymbol{R}(\boldsymbol{X},\boldsymbol{W}) - \boldsymbol{S} = \tilde{\boldsymbol{R}}(\boldsymbol{X},\boldsymbol{W},\boldsymbol{S}) = 0\,. \tag{1}$$

As the forces applied to the flow are modeled for each engine row, blades are not meshed. Therefore, the body-force mesh is far simpler and smaller in size than its blade-resolved counterpart, thus reducing the memory and CPU wallclock-time needed to undertake the simulation. Besides, the body-force computation can remain stationary even under inlet distortions.

Explicit body-force models intend to analytically evaluate the blade force applied to the fluid, based on the local flow variables $\boldsymbol{W}$ and the engine parameters $\boldsymbol{\beta}$. These ones can include both operating parameters, like rotational speed or total thrust, as well as blade shape parameters, depending on the considered model. Consequently, the functional dependencies of the source terms can be expressed as $\boldsymbol{S} = \boldsymbol{S}(\boldsymbol{X},\boldsymbol{W},\boldsymbol{\beta})$. Considering the absence of a blade metal blockage modeling and neglecting any contribution to the turbulence model, the general expression of $\boldsymbol{S}$ is given by

$$\boldsymbol{S} = \begin{Bmatrix} \boldsymbol{S}_\rho \\ \overrightarrow{\boldsymbol{S}_{\rho v}} \\ \boldsymbol{S}_{\rho E} \\ \boldsymbol{S}_{\tilde{\nu}} \end{Bmatrix} = \begin{Bmatrix} 0 \\ \boldsymbol{\rho}\overrightarrow{\boldsymbol{f}} \\ \boldsymbol{\rho}\overrightarrow{\boldsymbol{f}}\cdot\overrightarrow{\boldsymbol{v}} \\ 0 \end{Bmatrix}, \tag{2}$$

where $\overrightarrow{\boldsymbol{v}}$ stands for the local absolute velocity vector and $\boldsymbol{\rho}$ stands for the local flow density.

A. The Hall-Thollet's model

Considering advanced explicit BFM models, like the Hall-Thollet's model [5, 8], some hypothesis on the inlet distortion patterns and the pressure distribution along the blade skin are needed to compute the source terms. Indeed, for such a model, one must consider a single blade-to-blade row channel, perform a pitch-wise average of the blade aerodynamic load and smear it out circumferentially. The obtained equations are used to build up a model of the local blade force relying on both the local flow and the blade shape variables. As consequences, the source term computation is purely local. The model provides a good approximation of the time-averaged engine flow quantities and performance, dealing with both rotor and stator blade rows, as shown in [8] and in [4]. These source terms are expected to reproduce the enthalpy and entropy rise across any blade wheel, based on the local flow state.

The Hall-Thollet's model can be conveniently expressed in the cylindrical coordinate system $(\overrightarrow{e_x},\overrightarrow{e_\theta},\overrightarrow{e_r})$ associated to a blade row rotating around its axis $\overrightarrow{e_x}$. We denote by $\overrightarrow{v_{rot}}$ the flow velocity in the blade row rotating frame of reference. The blade force $\overrightarrow{f}$ can be split in two contributions regarding the local relative flow velocity $\overrightarrow{v_{rot}}$. The first, denoted $\overrightarrow{f_p}$, is parallel and opposite to $\overrightarrow{v_{rot}}$, along the unitary vector $\overrightarrow{e_p}$. The second, denoted $\overrightarrow{f_n}$, is normal to both $\overrightarrow{v_{rot}}$ and $\overrightarrow{e_r}$ and oriented along the unitary vector $\overrightarrow{e_n} = \overrightarrow{e_p} \wedge \overrightarrow{e_r}$, with $\wedge$ the vectorial product.

$$\overrightarrow{e_p} = -\frac{\overrightarrow{v_{rot}}}{\left\|\overrightarrow{v_{rot}}\right\|}\,, \tag{3}$$

$$\text{and } \overrightarrow{f} = \overrightarrow{f_n} + \overrightarrow{f_p} = f_n\overrightarrow{e_n} + f_p\overrightarrow{e_p}\,. \tag{4}$$

We denote by $\overrightarrow{\eta_{skel}}$ the unitary vector normal to the blade camber-surface - chosen so that for a flat plate without pitch $\overrightarrow{\eta_{skel}} = \overrightarrow{e_\theta}$ - and by δ the local flow deviation, defined as the oriented angle between the plane locally tangent to the blade surface and $\overrightarrow{v_{rot}}$. Thus we define the unitary vector $\overrightarrow{e_n}$ and the flow velocity component tangent to the camber-surface $\overrightarrow{v_p}$ as follows:

$$\overrightarrow{v_p} = \overrightarrow{v_{rot}} - \left(\overrightarrow{v_{rot}}.\overrightarrow{\eta_{skel}}\right)\overrightarrow{\eta_{skel}}\,, \tag{5}$$

$$\text{and } \overrightarrow{e_n} = \cos(\delta)\overrightarrow{\eta_{skel}} - \sin(\delta)\frac{\overrightarrow{v_p}}{\left\|\overrightarrow{v_p}\right\|}\,. \tag{6}$$

These unitary vectors are schematized in Figure 1.

In this model proposed by Hall [5] in 2015, the blade force normal component model relies directly on blade shape parameters - i.e. the normal to the local camber-surface $\overrightarrow{\eta_{skel}}$ and the local blade-to-blade passing channel height $\boldsymbol{H}$ - through a thin-airfoil approximation. In 2017, Thollet's [8] introduced a Prandtl-Ackeret compressibility correction to

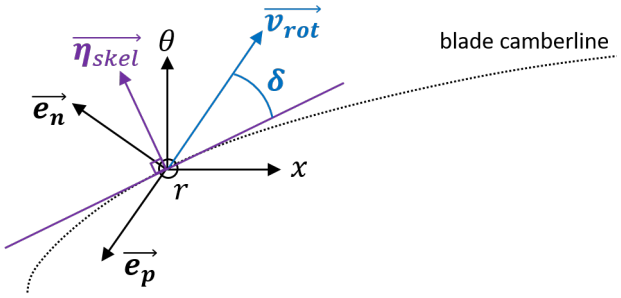

Fig. 1 2D schematic of the unitary vectors used for the blade force decomposition regarding the blade camberline and the local flow deflection.

take into account some of the transonic compressibility effects and added a parallel component to empirically model the losses. The resulting expression of the Hall-Thollet normal and parallel force components are given by:

$$f_n = \underbrace{\kappa^*(M)}_{\text{compressibility correction}} * \frac{1}{2}\left\|\overrightarrow{v}\right\|^2 2\pi \frac{\delta}{H\left\|\overrightarrow{\eta_{skel}}\cdot\overrightarrow{e_\theta}\right\|}\,, \tag{7}$$

$$f_p = \underbrace{\kappa^*(M)}_{\text{compressibility correction}} * \left[\underbrace{K_p}_{\text{viscous losses model}} + \underbrace{2\pi\left(\delta-\delta_{\eta_{max}}\right)^2}_{\text{quadratic losses model}}\right] * \frac{\left\|\overrightarrow{v}\right\|^2}{2H\left\|\overrightarrow{\eta_{skel}}\cdot\overrightarrow{e_\theta}\right\|} \tag{8}$$

$$\text{with:}\quad \kappa(M) = \begin{cases} \dfrac{1}{\sqrt{1-M^2}} \text{ if } M \le 1.0 \\ \dfrac{4}{2\pi\sqrt{M^2-1}} \text{ if } M \ge 1.0 \end{cases} \quad \text{and: } \kappa^*(M) = \min(\kappa(M);3)\,, \tag{9}$$

where M stands for the local flow Mach number, while K_p and $\delta_{\eta_{max}}$ are calibration coefficients to improve the model accuracy. The quadratic losses model is introduced to mitigates the lack of precision of the model at low mass flow rates and to reproduce a parabolic shape of the fan efficiency with respect to the mass flow [8]. The viscous losses model is made to match this parabolic curve to the actual efficiency trend. $\delta_{\eta_{max}}$ is the flow deflection extracted from a body-force simulation at maximum efficiency - the maximum efficiency operating point must however been determined using high-fidelity simulations - and K_p is determined to match the maximum efficiency value obtained with the high fidelity simulations. With those modifications, the model is able to correctly reproduce the engine performance, even under inlet distorted conditions. Since the analytic expression depends on the blade skeleton geometry, it can give access to a great number of degrees of freedom for the engine design study. Besides, the sensitivity analysis through the body-force adjoint may enhance our understanding of aero-propulsive coupling mechanisms and provide some good design practices when studying strongly coupled aero-propulsive configurations.

In preliminary design, K_p can be estimated through a flat-plate friction coefficient analogy [4, 8]. Besides, when considering the optimization of the blade geometry, it can be challenging to recalibrate the Hall-Thollet's model for each new design, taking into account the calibration contribution into the QoI sensitivities. Since the optimizer will primarily need the accurate engine performance trends, it is possible, in a first attempt, to reduce the quadratic loss model to $2\pi\delta^2$, meaning the losses are scaling quadratically with the local misalignment between the fluid en the blade camber surface. At first, only this component of the parallel force is implemented. The considered model, denoted as Quadratic Not Calibrated (QNC) from now on, is thus reduced to the following expressions:

$$f_n = \frac{1}{2}\left\|\overrightarrow{v}\right\|^2 2\pi \frac{\delta}{H\left\|\overrightarrow{\eta_{skel}}\cdot\overrightarrow{e_\theta}\right\|}\,, \tag{10}$$

$$f_p = 2\pi\delta^2 * \frac{\left\|\overrightarrow{v}\right\|^2}{2H\left\|\overrightarrow{\eta_{skel}}\cdot\overrightarrow{e_\theta}\right\|}\,. \tag{11}$$

The body-force implementations, as well as the QoIs implementation and their respective adjoint formulation, are undertaken in an in-house BFM library called *BACARDI* [25]. This library is interfaced with the modernized module

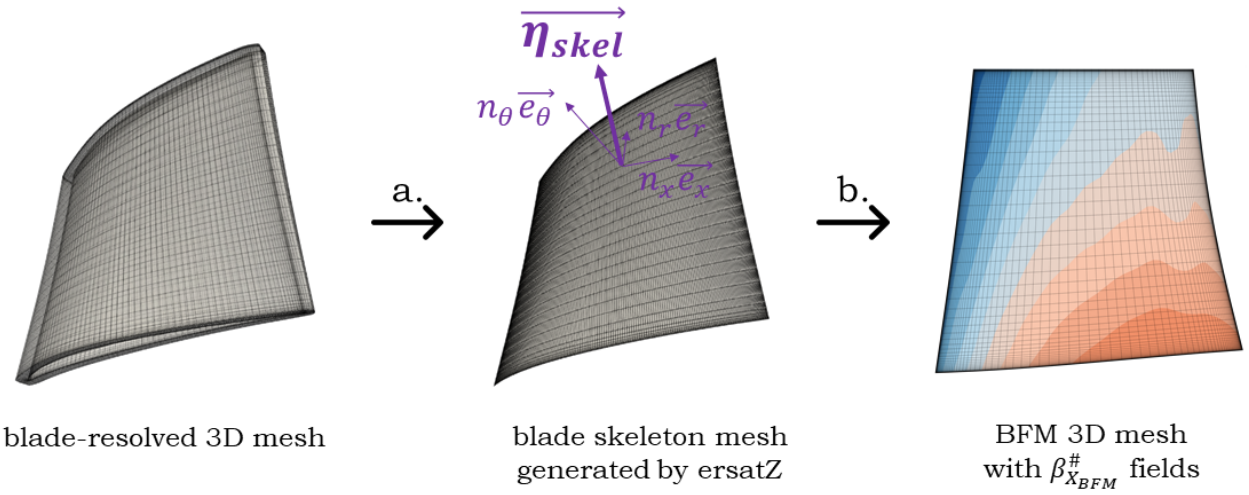

Fig. 2 Schematic of the process to generate the $\beta^{\#}_{X_{BFM}}$ *BACARDI* input fields. a: extraction of the blade skin coordinates from the blade-resolved mesh, computation of the blade skeleton coordinates with ersatZ, with its own surface discretization. The cylindrical normal components of the normal to the blade skeleton are then computed at each face center of the skeleton mesh. b: interpolation of these surface fields from the skeleton mesh on the BFM mesh, based on the axial and radial coordinates.

[26] of the *elsA* software [22] (ONERA-SAFRAN property). The inputs of the *BACARDI* module, denoted $\beta^{\#}_{X_{BFM}}$ in general, are, for the Hall normal force and for each blade wheel, its rotational speed Ω, its total number of blades N, and the component fields of the normal to the blade skeleton in the cylindrical coordinate systems, denoted n_x, n_θ and n_r, respectively. In the general case, the body-force parameter field $\beta^{\#}_{X_{BFM}}$ is the result of the body-force parametrization process, which takes the engine design parameters β and the body-force mesh X_{BFM} as inputs. For the Hall model, the process generating these $\beta^{\#}_{X_{BFM}}$ fields is schematized in Figure 2. The process takes as input the mesh with discretized blade geometries, analyzes it and computes the skeleton (or camber surface) of each blade row, using the ONERA's in-house blade parametrization tool ersatZ. Then, the normal field is computed on this skeleton. The three normal component fields are then interpolated from the blade skeleton surface to the 3D body-force mesh. In that process, the body-force mesh X_{BFM} fits the edges of the blade skeleton projection in the meridional plane. We will designate it as a blade-fitted body-force mesh.

For Ω and N, the body-force variable β is a scalar duplicated in each cells of the mesh of the given row to produce the body-force parameter field $\beta^{\#}_{X_{BFM}}$. Therefore, we have the basic relations :

$$\beta^{\#}_{X_{BFM}} = \mathbb{1} * \beta \,, \tag{12}$$

where $\mathbb{1}$ stands for a unitary field of the same shape as W.

B. Adjoint body-force formulation

Enhancing the propulsive system performance through an optimization of the engine parameters β requires to deal with a potentially large number of design variables and a small number of functions of interest. Therefore, the adjoint methodology is of great interest to compute precisely and efficiently the associated gradients [27]. In the *elsA* software, a discrete adjoint implementation of the CFD solver is available [23, 28]. The legacy adjoint implementation allows to compute the sensitivities of a function of interest $\mathcal{J}(X, W)$ when the steady state is reached, meaning $R(X, W) = 0$. If the propulsive system is modelled thanks to an explicit BFM, the adjoint equations must be re-written to take into account the body-force source term contribution to the adjoint vector and to the QoI gradients. In that case, considering that any QoI may involve the body-force source terms in its formulation, we can express the gradient of any QoI

$\mathcal{J}(\boldsymbol{X}, \boldsymbol{W}, \boldsymbol{\beta})$ with respect to the engine design parameters $\boldsymbol{\beta}$ at residual convergence $\tilde{\boldsymbol{R}}(\boldsymbol{X}, \boldsymbol{W}, \boldsymbol{S}) = 0$ as follows:

$$\frac{d\mathcal{J}}{d\boldsymbol{\beta}} = \frac{\partial \mathcal{J}}{\partial \boldsymbol{X}}\frac{d\boldsymbol{X}}{d\boldsymbol{\beta}} + \frac{\partial \mathcal{J}}{\partial \boldsymbol{W}}\frac{d\boldsymbol{W}}{d\boldsymbol{\beta}} + \frac{\partial \mathcal{J}}{\partial \boldsymbol{\beta}}\,, \tag{13}$$

$$\frac{d\tilde{\boldsymbol{R}}}{d\boldsymbol{\beta}} = \frac{\partial \boldsymbol{R}}{\partial \boldsymbol{X}}\frac{d\boldsymbol{X}}{d\boldsymbol{\beta}} + \frac{\partial \boldsymbol{R}}{\partial \boldsymbol{W}}\frac{d\boldsymbol{W}}{d\boldsymbol{\beta}} \underbrace{- \frac{\partial \boldsymbol{S}}{\partial \boldsymbol{X}}\frac{d\boldsymbol{X}}{d\boldsymbol{\beta}} - \frac{\partial \boldsymbol{S}}{\partial \boldsymbol{W}}\frac{d\boldsymbol{W}}{d\boldsymbol{\beta}} - \frac{\partial \boldsymbol{S}}{\partial \boldsymbol{\beta}}}_{\text{additional contributions due to the BFM source terms}} = 0\,. \tag{14}$$

(15)

Let us introduce the body-force adjoint equations:

$$\left(\frac{\partial \tilde{\boldsymbol{R}}}{\partial \boldsymbol{W}}\right)^T \tilde{\boldsymbol{\Lambda}} = -\frac{\partial \mathcal{J}}{\partial \boldsymbol{W}}\,, \tag{16}$$

$$\text{or:} \left(\frac{\partial \boldsymbol{R}}{\partial \boldsymbol{W}} - \underbrace{\frac{\partial \boldsymbol{S}}{\partial \boldsymbol{W}}}_{\text{BFM contribution}}\right)^T \tilde{\boldsymbol{\Lambda}} = -\frac{\partial \mathcal{J}}{\partial \boldsymbol{W}}\,. \tag{17}$$

We can observe that the BFM adds a contribution to the adjoint system. Then, by multiplying eq. (14) by $\tilde{\boldsymbol{\Lambda}}^T$, adding it to eq. (13) and substituting from eq. (17), we obtain the following gradient expression:

$$\frac{d\mathcal{J}}{d\boldsymbol{\beta}} = \underbrace{\left(\frac{\partial \mathcal{J}}{\partial \boldsymbol{X}} + \tilde{\boldsymbol{\Lambda}}^T\frac{\partial \tilde{\boldsymbol{R}}}{\partial \boldsymbol{X}}\right)\frac{d\boldsymbol{X}}{d\boldsymbol{\beta}}}_{\substack{\text{BFM mesh}\\ \text{sensitivities}}} + \underbrace{\left(\frac{\partial \mathcal{J}}{\partial \boldsymbol{\beta}} + \tilde{\boldsymbol{\Lambda}}^T\frac{\partial \tilde{\boldsymbol{R}}}{\partial \boldsymbol{\beta}}\right)}_{\substack{\text{BFM direct}\\ \text{sensitivities}}}\,. \tag{18}$$

The *BACARDI* module gives access to the analytical sensitivities of $\mathcal{J}$ with respect to the $\boldsymbol{\beta}^{\#}_{\boldsymbol{X}_{BFM}}$ parameters, ie:

$$\left.\frac{d\mathcal{J}}{d\boldsymbol{\beta}^{\#}_{\boldsymbol{X}_{BFM}}}\right|_{\boldsymbol{X}_{BFM}} = \frac{\partial \mathcal{J}}{\partial \boldsymbol{\beta}^{\#}_{\boldsymbol{X}_{BFM}}} + \tilde{\boldsymbol{\Lambda}}^T\frac{\partial \tilde{\boldsymbol{R}}}{\partial \boldsymbol{\beta}^{\#}_{\boldsymbol{X}_{BFM}}}\,,$$

which is a cell-center vector of the same shape than $\boldsymbol{W}$. In a general case, the functional dependencies of $\boldsymbol{\beta}^{\#}_{\boldsymbol{X}_{BFM}}$ reads:

$$\boldsymbol{\beta}^{\#}_{\boldsymbol{X}_{BFM}}(\boldsymbol{\beta}, \boldsymbol{X}_{BFM})\,,$$

$$\text{and thus:}\quad \frac{\partial \mathcal{J}}{\partial \boldsymbol{\beta}} + \tilde{\boldsymbol{\Lambda}}^T\frac{\partial \tilde{\boldsymbol{R}}}{\partial \boldsymbol{\beta}} = \left(\frac{\partial \mathcal{J}}{\partial \boldsymbol{\beta}^{\#}_{\boldsymbol{X}_{BFM}}} + \tilde{\boldsymbol{\Lambda}}^T\frac{\partial \tilde{\boldsymbol{R}}}{\partial \boldsymbol{\beta}^{\#}_{\boldsymbol{X}_{BFM}}}\right)\left.\frac{\partial \boldsymbol{\beta}^{\#}_{\boldsymbol{X}_{BFM}}}{\partial \boldsymbol{\beta}}\right|_{\boldsymbol{X}_{BFM}} \tag{19}$$

To retrieve the BFM direct sensitivity contribution to $\dfrac{d\mathcal{J}}{d\boldsymbol{\beta}}$, one must then compute the partial derivatives of the body-force discretized fields with respect to each body-force control parameter $\boldsymbol{\beta}$, while keeping the body-force mesh unmodified. If the body-force parametrization process is not adjoint-compatible, the evaluation of $\left.\dfrac{\partial \boldsymbol{\beta}^{\#}_{\boldsymbol{X}_{BFM}}}{\partial \boldsymbol{\beta}}\right|_{\boldsymbol{X}_{BFM}}$ can be done through finite-differences.

If one considers an engine parameter $\boldsymbol{\beta}$ affecting only the input fields of *BACARDI* $\boldsymbol{\beta}^{\#}_{\boldsymbol{X}_{BFM}}$, then only the direct BFM sensitivities of equation (13) contributes to the gradient. This is the case, for instance, for the fan rotational speed Ω as input of *BACARDI*. On the contrary, blade shape parameters, like the blade chord, affect the skeleton meridional projection, and therefore requires a deformation of the blade-fitted body-force mesh. As consequences, both components of eq. (13) must be considered in the total gradient of $\mathcal{J}$ with respect to $\boldsymbol{\beta}$.

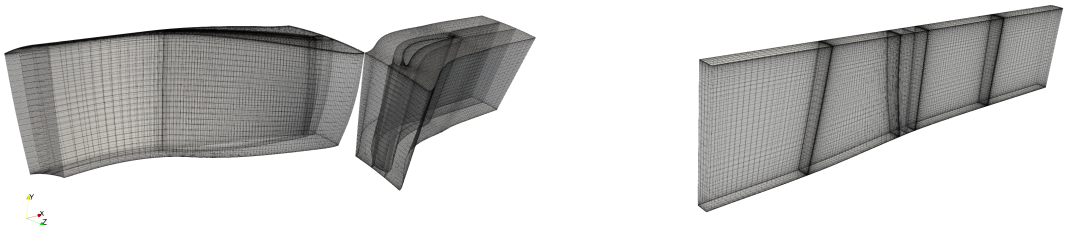

(a) RANS CME2 single blade passage mesh **(b) BFM mesh counterpart**

Fig. 3 Geometry of the CME2 single blade passage channel and its associated RANS and BFM meshes.

IV. Hall model primal and adjoint validation

A. The CME2 compressor

As explained in section III.A, the body-force model proposed by Hall [5] has proven able to reproduce the engine performance trends based on the local values of the flow conservatives and on the blade skeleton normal. Godard's work [6] also suggests that this model may be relevant for preliminary fan design under significant inlet distortions. In the context of an aero-propulsive optimization, such a model is expected to offer a precise feedback on the engine efficiency and on its power consumption when altering the airframe shape, thanks to an internal flow simulation of higher fidelity than other throughflow models [8]. The adjoint formulations of both the Hall model without losses (denoted HNL from now on) and the QNC extension have been implemented in *BACARDI*, and we present here their validation. This work provides access to the sensitivities of the engine performance metrics with respect to the blade shape parameters. In the context of an aero-propulsive optimization, this new tool will also provides access to the contribution of the engine model sensitivities to the airframe shape gradients.

For the purpose of the Hall model primal and adjoint implementations validation, we consider a single blade passage geometry of the ONERA's CME2 compressor. The configuration consists of two rows of blades, with a single fan blade over the 30 of the full configuration and a single stator blade over 40. The blade-resolved and body-force meshes are respectively presented in Figures 3a and 3b. The body-force mesh is generated from its blade-resolved counterpart and features a cell size of 10^{-6} m at the walls and of 10^{-5} m at the rows leading and trailing edges. Additional information on the BFM mesh generation is given in section IV.E.

For all this study, inlet conditions remain unchanged and feature a total temperature $T_{i_{\text{IN}}} = 288.15$ K, a total pressure $P_{i_{\text{IN}}} = 101\,325$ Pa and a Mach number $M_{\text{IN}} = 0.287$. The fan rotation speed considered here is 6 400 RPM, close to the compressor design speed. Viscous wall boundary conditions are imposed at the hub and shroud. Periodic boundary conditions are imposed at the sides of the channel. The Spalart-Allmaras turbulence model was used for this test case, using its negative formulation for the body-force simulations. The convective fluxes are discretized using the Roe scheme. The discrete viscous fluxes are computed based on cell-centered gradients corrected at the interface in the direction of the two adjacent centers. The blade-resolved simulation makes use of a mixing plane interface condition between the rotor and the stator channels. The blade-resolved mesh is structured, while its body-force counterpart is topologically structured but described as unstructured. The latter is a meridional mesh extruded in the azimuthal direction over four cells and 2° around the compressor axis.

Studies on the blade-resolved mesh are carried out using the 'legacy' modules of *elsA* [22], whiles the body-force computations are performed using the modernized module of *elsA* [26].

B. Hall-Thollet primal implementation validation

To validate the primal implementation of both the HNL and the QNC versions of the Hall-Thollet model, we compute the engine performance characteristic using a radial equilibrium outlet condition associated with a quadratic valve law, which allows us to vary its pivot pressure. The engine characteristics are calculated for both the body-force models considered and for the blade-resolved RANS case. The results are shown in Figure 4. Π stands for the compression ratio of the whole stage, and η for the compressor isentropic efficiency. Results for the normal force of the Hall model without losses are drawn in red, while those of the QNC model are drawn in blue. Finally, 'Bladed' stands for the blade-resolved RANS simulations and are drawn in black. Blade-resolved simulations would not converged below $\dot{m} = 9$ kg.s^{-1}, which appears to be the compressor stability limit, where the flow periodicity over each blade-to-blade

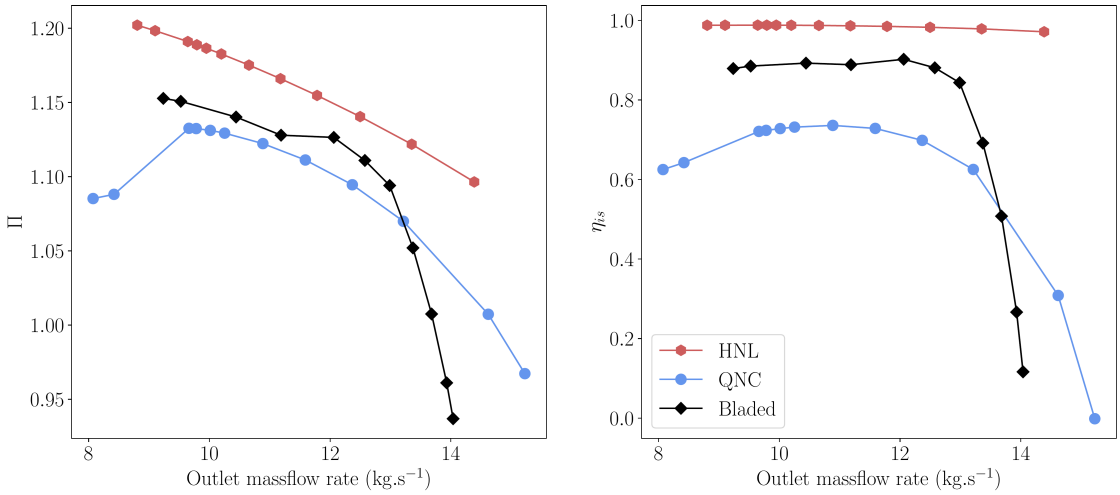

Fig. 4 Engine characteristics at 6400 RPM, in red for the Hall model, in blue for the Hall model with not calibrated quadratic losses, and in black for the blade-resolved RANS simulations.

channel hypothesis may no longer be valid. Near max efficiency, ie with $\dot{m}$ between 10 and 12 kg.s^{-1}, we observe a good agreement between the Hall model without losses and the blade-resolved results. This body-force model overestimates the compression ratio as well as the compressor isentropic efficiency but the trends are correctly captured in that part of the characteristic. However, at low and at high mass flow rates, the predictions are incorrect. The body-force model cannot capture the compressor stability limit, and hence the expected $(\dot{m}, \Pi)$ positive slop at low mass flow rates, and neither the blockage near 14 kg.s^{-1}. On the contrary, the Hall model with not calibrated quadratic losses can correctly capture the compressor performance trends at low mass flow rates and assess rather correctly the compressor stability limit. It also performs better near the blockage even if the slope of the $(\dot{m}, \Pi)$ and the $(\dot{m}, \eta)$ curves are significantly underestimated. As consequences, the maximum mass flow rate is overestimated. Enhancing the model accuracy in that region may require the implementation of the blade metal blockage model proposed by Kottapalli [29] in 2013. Since the quadratic losses are not calibrated, they are overestimated, resulting in an underestimation of both the compression ratio and the efficiency of the overall compressor characteristic. As the gradients primarily need the correct trends, this correction may appear sufficient to perform compressor pre-design optimizations.

C. Hall-Thollet adjoint implementation validation

We present in this section a first validation of the adjoint implementation of the Hall normal force with non calibrated quadratic losses. We validate the direct body-force sensitivities of the power delivered by the fan $\mathcal{Q}_{POW}$ to each of the *BACARDI* inputs, and therefore indirectly the adjoint vector $\tilde{\mathbf{\Lambda}}$ solution of eq. (17) by comparing them against centered finite-differences. For Ω and N, since the $\boldsymbol{\beta}^{\#}_{\boldsymbol{X}_{BFM}}$ field consists of a scalar duplicated in each cells of the mesh of the given row, the sensitivities of $\boldsymbol{\beta}^{\#}_{\boldsymbol{X}_{BFM}}$ with respect to $\boldsymbol{\beta}$ simplifies as :

$$\left.\frac{\partial \boldsymbol{\beta}^{\#}_{\boldsymbol{X}_{BFM}}}{\partial \boldsymbol{\beta}}\right|_{\boldsymbol{X}_{BFM}} = \mathbb{1} \, . \tag{20}$$

For body-force computations, $\mathcal{Q}_{POW}$ can be easily computed, using *BACARDI*, by integrating the body-force energy source terms:

$$\mathcal{Q}_{POW}(\boldsymbol{X}, \boldsymbol{W}, \boldsymbol{S}) = - \iiint_{V_{BFM}} \boldsymbol{S}_{\rho E}(\vec{\boldsymbol{f}}) dV \, . \tag{21}$$

We choose this QoI for our study, since it has proven relevant as aero-propulsive optimization objective function in previous studies. *BACARDI* also provides the sensitivities of this function with respect to the flow conservatives and the body-force input parameters. For the blade-resolved simulations, this quantity and its sensitivities can be evaluated using the dedicated ONERA's in-house post-processing module.

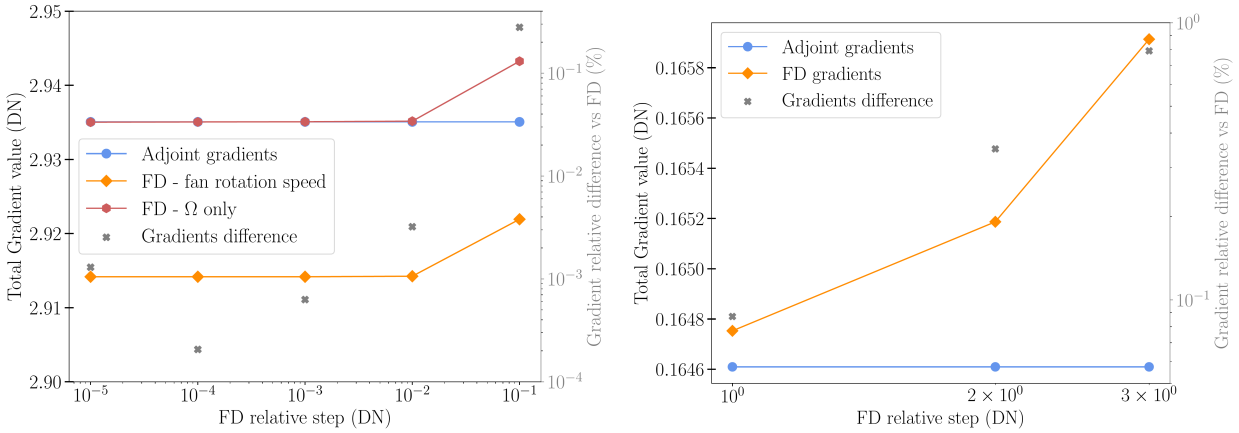

(a) Validation of the BFM sensitivities w.r.t. Ω **(b) Validation of the BFM sensitivities w.r.t. *N***

Fig. 5 Validation of the ABFM analytical gradients through a centered FD convergence, for the Ω and *N* parameters of the Hall model. For Figure a, the gradient relative difference against finite-differences are computed based on the FD results drawn in red.

We select an operating point in the stable region of the engine characteristic, far from the blockage and the stability limit, i.e. in the engine operating region, near $\dot{m} \approx 12$ kg.s^{-1}. Since the radial equilibrium is not yet differentiated in the modernized *elsA* module, we need to find the outlet static pressure map leading to this mass flow rate. Based on the blade-resolved simulations, we assessed that such mass flow rate was obtained for an outlet pressure condition of $P_{out} = 107\,400$ Pa. We performed a blade-resolved simulation with this outlet condition and measured an outlet mass flow rate of 12.0778 kg.s^{-1} for the equivalent 360° configuration. Then, we used a radial equilibrium outlet condition with a valve law enforcing the same full-annulus outlet mass flow rate in the body-force data setting to obtain the static pressure map associated to this operating condition. We finally performed the body-force simulations, QoIs evaluations and gradients computations using this outlet static pressure map. Body-force simulations were conducted with the QNC losses model, with all cell density residuals converged below 10^{-13} kg.m^{-3}. The same pressure map was used for the finite-differences gradient evaluations.

The validation of these adjoint sensitivities against centered finite-differences are shown in 5a for Ω and in 5b for N, where we can see a good agreement. Gradients were made dimensionless by dividing them by the full-annulus power consumption evaluated with *BACARDI* on body-force simulations, and multiplying them by the scaling factor of the design variable. For the fan rotational speed, two sets of finite-differences gradients were computed. In the first set, in orange, both the *BACARDI* input Ω and the hub wall boundary condition rotation speed were modified. In the second, in red, only the *BACARDI* input Ω was altered. The scaling factor of the design variable considered here is the fan rotation speed, i.e. 6400 RPM. The convergence of the red curve on the adjoint gradient, in blue, confirms the *BACARDI* adjoint formulation is correct for this input parameter. The second convergence curve shows a small offset with the adjoint gradient, of about 0.7% of its value. Indeed, *BACARDI* does not take into account the hub wall boundary condition sensitivities with respect to the fan rotation speed into the sensitivity field it provides for Ω, since this boundary condition parameter is not involved in the body-force model formulation. Therefore, this offset can be interpreted as the error made on the gradient of $\mathcal{Q}_{POW}$ with respect to the fan rotation speed if it is considered equal to the gradient of $\mathcal{Q}_{POW}$ with respect to the *BACARDI* input parameter Ω. Thus, it appears the sensitivity of $\mathcal{Q}_{POW}$ with respect to the hub wall rotation speed can be neglected compared to the $\mathcal{Q}_{POW}$ sensitivities with respect to the body-force input parameter Ω. In a coupled aero-propulsive optimization, the fan rotation speed can thus be modified based only on the gradient directly provided by *BACARDI* for this parameter, with still a very good precision. For N, we can clearly see that the finite-differences gradients are converging towards the adjoint, but since the number of blades must be an integer for *BACARDI*, smallest steps could not be attempted to observe a full convergence. The scaling factor of the design variable considered here is the fan blades number, i.e. 30.

Contrary to Ω and N, the normal to the blade skeleton fields are non-linearly affected by many blade shape parameters, like local camber or chord modifications. The relation between the blade shape parameters and the blade skeleton coordinates can be establish through a blade shape parametrization tool, like ersatZ. Then, one must evaluate the normal

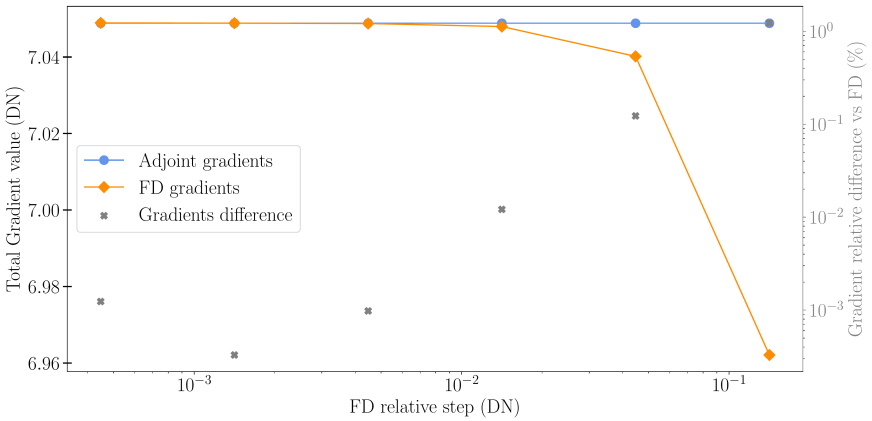

Fig. 6 Validation of the sensitivities of Q_{POW} with respect to the normal fields components n_x and n_θ through the variable σ.

coordinates to this skeleton and interpolate it on the associated row's body-force mesh. To compute $\left.\frac{\partial \beta^{\#}_{X_{BFM}}}{\partial \beta}\right|_{X_{BFM}}$, finite-differences must be used since ersatZ doesn't have been differentiated. As consequences, the sensitivity assembly is complex. At first, we can perform a direct numerical validation of the volume sensitivities provided by *BACARDI* - and thus indirectly of the adjoint solution it provides - for the normal to the blade skeleton fields. We consider a simplified and purely local deformation to overcome the need for a blade parametrization tool. To do so, a rotation matrix is applied on the normal components, in order to preserve their unitary modulus, in each cell of the body-force mesh. This purely numerical deformation can be interpreted as a rotation of each face of the blade skeleton mesh over their barycenter, and does not correspond to a pitch deformation of the blade. Therefore, each cell-centered values of the normal component fields after the rotation of angle σ simply read :

$$\begin{bmatrix} n_x(\sigma) \\ n_\theta(\sigma) \\ n_r(\sigma) \end{bmatrix} = \begin{bmatrix} \cos(\sigma) & \sin(\sigma) & 0 \\ -\sin(\sigma) & \cos(\sigma) & 0 \\ 0 & 0 & 1 \end{bmatrix} \times \begin{bmatrix} n_x \\ n_\theta \\ n_r \end{bmatrix} \tag{22}$$

As we compute the gradients for $\sigma = 0$ rad, the sensitivities of Q_{POW} to σ simply reads:

$$\frac{dQ_{POW}}{d\sigma} = \frac{\partial Q_{POW}}{\partial n_x} n_\theta - \frac{\partial Q_{POW}}{\partial n_\theta} n_x \tag{23}$$

The results for this validation are given in Figure 6. Gradients were made dimensionless using π rad as the design variable scaling coefficient. Again, we observe a very good match between the adjoint and the finite differences gradients, with a minimal relative difference below 0.001% before the onset of the truncation error, which appears for relative steps lower than 0.001.

D. Hall-Thollet fan shape gradients validation

Second, we can perform a finite-differences validation of the gradients of Q_{POW}, using real blade shape parameters via the ersatZ tool. We evaluate the gradients of the Q_{POW} function for 10 camber control points on the fan skeleton, placed at the leading and trailing edges, respectively at 0, 25, 50, 75 and 100% of the channel height. We denote by $\beta^{row}_{hX\,mY}$ the camber control point, placed on the skeleton of the row row, at the relative channel height $h = X$% and the relative chord position $m = Y$%. Those control points, depicted in Figure 7a, enable us to control locally the camber of the blade skeleton. The camber deformation is performed ensuring the conservation of the blade chord. As a result, the meridional projection of the blade chord is affected by these deformations, as well as the meridional projections of both the blade leading and trailing edge lines. Consequently, the body-fitted body-force mesh must be deformed, and the body-force mesh sensitivities of eq. (18) must be taken into account in the total gradient of Q_{POW} with respect to each control points.

The modernized *elsA* module cannot yet assemble the partial derivatives of any $\mathcal{J}$ and $\tilde{\boldsymbol{R}}$ with respect to the mesh coordinates $\boldsymbol{X}$ (see eq. (18)). Therefore, a methodology has been implemented to assemble the sensitivities of $\mathcal{J}$ with respect to the shape variables, using the solution vector $\tilde{\boldsymbol{\Lambda}}$ of the ABFM adjoint equations given in (17). This methodology consists of producing, for each shape variable $\boldsymbol{\beta}$, two deformed meshes $\boldsymbol{X} + \Delta X$ and $\boldsymbol{X} - \Delta X$, interpolating the primal flow solution $\boldsymbol{W}_{primal}$ on those and measuring the QoI $\Delta\mathcal{J}$ and residuals $\Delta\tilde{\boldsymbol{R}}$ variations due to pure geometrical contribution. The mesh sensitivities can then be assembled as follows, to be added to the BFM sensitivities in order to obtain the full gradient:

$$\left.\frac{d\mathcal{J}}{d\boldsymbol{\beta}}\right|_{\boldsymbol{\beta}^{\#}_{\boldsymbol{X}_{BFM}}} = \left.\frac{\Delta\mathcal{J}}{\Delta\boldsymbol{\beta}}\right|_{\boldsymbol{\beta}^{\#}_{\boldsymbol{X}_{BFM}}} + \tilde{\boldsymbol{\Lambda}}^{T}\left.\frac{\Delta\tilde{\boldsymbol{R}}}{\Delta\boldsymbol{\beta}}\right|_{\boldsymbol{\beta}^{\#}_{\boldsymbol{X}_{BFM}}} . \tag{24}$$

On the contrary, the direct BFM sensitivities can be analytically assembled, as mentionned in equ. 19. However, it requires to obtain accurate finite-differences of the normal to the blade skeleton $\overrightarrow{\boldsymbol{\eta}_{skel}}$, and to accurately interpolate those surfacic geometric sensitivity fields on the body-force mesh. This process was implemented and tested, however we observed a poor numerical precision of this partial derivative, mainly due to numerical imprecision introduced by the interpolation of the n_x, n_θ and n_r surfacic geometric sensitivity fields, defined on the skeleton, on the 3D body-force mesh. Additional work is necessary to obtain a satisfying process, precise and robust at the same time, which is mandatory to incorporate this new tool in an optimization framework. In the meantime, the adjoint-parameter sensitivity evaluation is used to assemble the total gradient of the QoI with respect to any blade shape parameter $\boldsymbol{\beta}$, i.e. with perturbations both on the body-force mesh and on the BACARDI input fields, as shown in equ. 25. This method has also proven very useful to challenge the numerical precision of the analytical body-force sensitivity assembly chain and may therefore serve as a validation tool in future applications.

$$\frac{d\mathcal{J}}{d\boldsymbol{\beta}} = \frac{\Delta\mathcal{J}}{\Delta\boldsymbol{\beta}} + \tilde{\boldsymbol{\Lambda}}^{T}\frac{\Delta\tilde{\boldsymbol{R}}}{\Delta\boldsymbol{\beta}} \tag{25}$$

Comparison between the adjoint-parameter and the finite-differences gradients are shown in Figure 7b. Adjoint-parameter gradients were evaluated using an absolute step on the camber control points of $0.1\,^\circ$ to generate the deformed geometries necessary for the gradient assembly, and are depicted in dots-filled bars. Finite-differences gradients were evaluated using the same absolute step, and are depicted in dashed-filled bars. The absolute values of the gradients relative difference, denoted $|\epsilon_{QNC}|$, are depicted in beige bars. Gradients were made dimensionless using a design variable scaling coefficient of 1° for each control point. We can observe once again a very good match between the two sets of gradients, with all relative difference absolute values below 0.1% of the gradient value.

E. Body-force mesh convergence

Before studying the ABFM gradient prediction accuracy, we must first assert, through a mesh convergence study, that both the QoIs evaluations and their gradients are not highly dependent on the body-force mesh refinement.

Body-force mesh generation The BFM mesh is generated from its blade-resolved counterpart. To do so, the block edges coordinates are extracted from the blade-resolved mesh and are used to generate a meridional mesh, divided in three blocks per blade row. The central mesh block fits the row blade skeleton projection in the meridional plane. A set of 6 parameters controls the refinement of this meriodional mesh :

- the number of points in the axial direction, for each block of the row, i.e upstream, central and downstream, respectively denoted $e_{c_{up}}$, $e_{c_{blade}}$ and $e_{c_{down}}$,
- the number of points in the radial direction $e_{c_{radial}}$,
- the size of the first cell at the hub and shroud walls $c_{s_{wall}}$,
- the size of the cells at the central block leading and trailing edges $c_{s_{edges}}$.

The point distribution is exponentially increasing when reaching the walls or the edges of the central block of each row. Then, this meriodinal mesh is azimuthaly extruded over a few degrees and a few number of mesh cells to be able to reproduce the 3D effects captured by the body-force, such as the swirl and the distortion transfer across the engine in the case of distorted inlet conditions. The number of cells along the azimuth and their refinement in that direction must be consistent with the inlet distortion pattern and with the model hypothesis. Since the Hall model rely

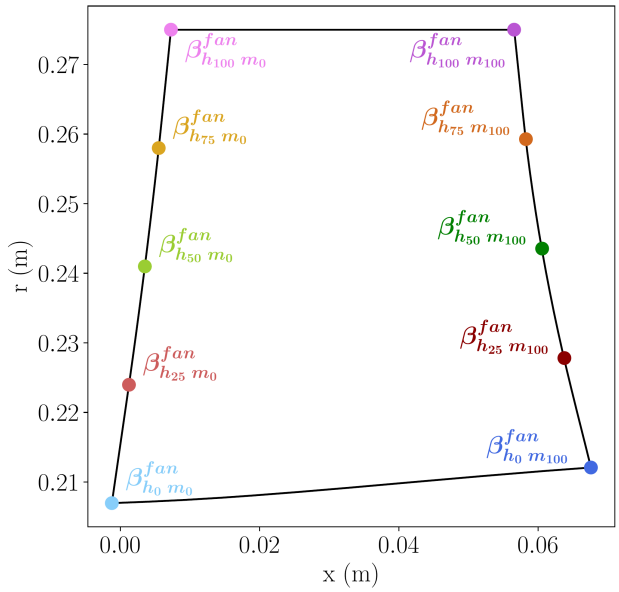

(a) Control points placed on the fan skeleton

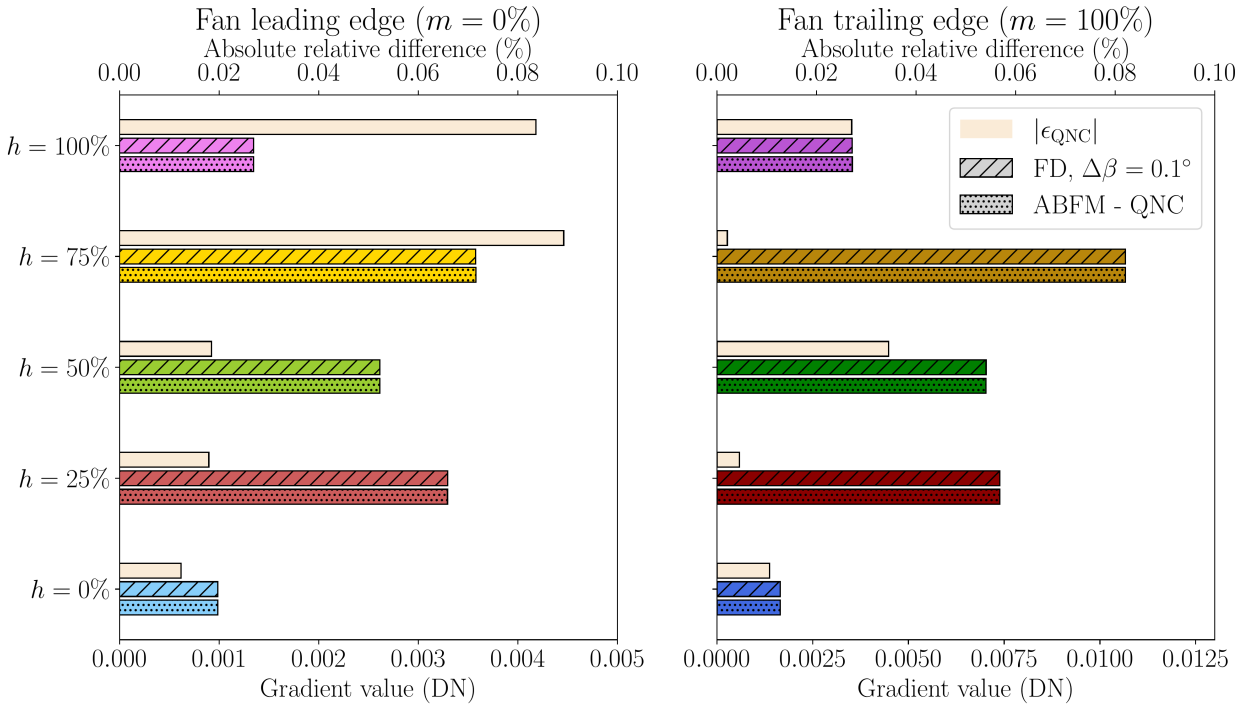

(b) Adjoint-parameter gradients validation

Fig. 7 Up: Meridional view of the camber control points placed on the fan skeleton. r stands for the radius and x for the axial position along the channel. Down : adjoint-parameter gradients validation against finite-differences. $|\epsilon_{QNC}|$ denotes the absolute values of the gradients relative difference, FD the finite-differnces results and ABFM-QNC the adjoint parameter results obtained with the QNC model.

Parameters		κ	N_{cells}	N_{bladed}/N_{cells}
Meshes	medium	1.0	139 784	8.73
	coarse	1.25	90 072	13.5
	fine	0.75	247 320	4.93

Table 1 Metrics of the three BFM mesh studied

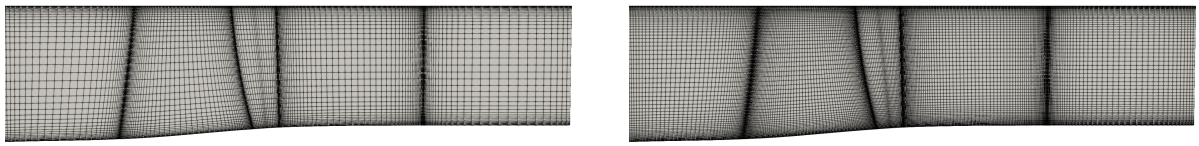

(a) Coarse mesh **(b) Fine mesh**

Fig. 8 Meridional view of the coarse and the fine mesh generated

on an inlet flow axial symmetry hypothesis over each blade-to-blade passage of the row [5], having a few cells in each blade-to-blade sector is consistent with the model hypothesis. In our case, the BFM mesh is the counterpart of a single blade passage mesh with discretized blades. The single blade passage configuration assumes a flow periodicity over each blade-to-blade channels. The BFM counterpart simulation therefore assumes a full-annulus axisymmetry of the flow, which is well represented by 4 cells along the azimuth over a small periodic sector of 2° for a CFD computation in the cartesian coordinates system. As consequences, in the mesh convergence study, the number of cells in that direction will remain constant.

We produce two body-force meshes, one coarser and one finer than the one used in the previous studies, denoted in this section as 'medium'. This mesh has been produced using the following parameters values:

- for the rotor, $e_{c_{up}} = 51$ and $e_{c_{down}} = 21$,
- for the stator $e_{c_{up}} = 21$ and $e_{c_{down}} = 51$,
- and for both rows $e_{c_{blade}} = 101$, $e_{c_{radial}} = 101$, $c_{s_{wall}} = 10^{-5}$ m and $c_{s_{edges}} = 10^{-6}$ m.

A scaling coefficient κ - respectively of 1.25 and 0.75 - is applied uniformly on each of the 6 parameters controlling the body-force mesh refinement. The parameters controlling the cell size are multiplied by κ, those controlling the number of points in the axial and radial directions are divided by κ. The obtained meshes are shown in Figure 8 and their metrics are given in Table 1. In the last column, the ratio between the number of cells of the blade-resolved mesh and the considered body-force mesh is given.

QoIs and QoI gradients variation with the mesh refinement We consider the same operating conditions and numerical methodology that the ones presented in IV.C for the gradients validation. In Table 2 we compare the evaluation of various QoIs on each BFM mesh. We denote respectively $\dot{m}_{IN}$ and $\dot{m}_{OUT}$ the inlet and outlet mass flow rates, $T_{i_{OUT}}/T_{i_{IN}}$ the total temperature ratio, $P_{i_{OUT}}/P_{i_{IN}}$ the total pressure ratio and P_{OUT}/P_{IN} the static pressure ratio and finally η the stage isentropic efficiency, for the equivalent full-annulus configuration.

We can clearly see that the refinement of the body-force mesh has almost no influence on the compressor performance quantities. Indeed, all variations observed are below 0.01% of the fine mesh value. The outlet mass flow rate $\dot{m}_{out}$ seems to be the quantity most sensible to the BFM mesh refinement.

We perform the same gradient evaluation on the coarse and the fine mesh than the one conducted in IV.C, using the adjoint-parameter method with a step on the camber control points amplitude of 0.1 °. Comparative results are shown in Figure 9. Again, we can see that the gradients are almost insensitive to the body-force mesh refinement. Given these results, we decide to follow the studies on the initial medium mesh, on which gradients validations were performed.

QoIs \ Evalution mesh	Coarse	Medium	Fine
$\dot{m}_{IN}$	12.076542	12.077050	12.077390
$\dot{m}_{OUT}$	12.076337	12.076907	12.077336
$T_{i_{OUT}}/T_{i_{IN}}$	1.040496	1.040487	1.040482
$P_{i_{OUT}}/P_{i_{IN}}$	1.104744	1.104727	1.104715
P_{OUT}/P_{IN}	1.101374	1.101358	1.101346
η	0.712901	0.712958	0.712947

Table 2 QoI variation with the level of mesh refinement.

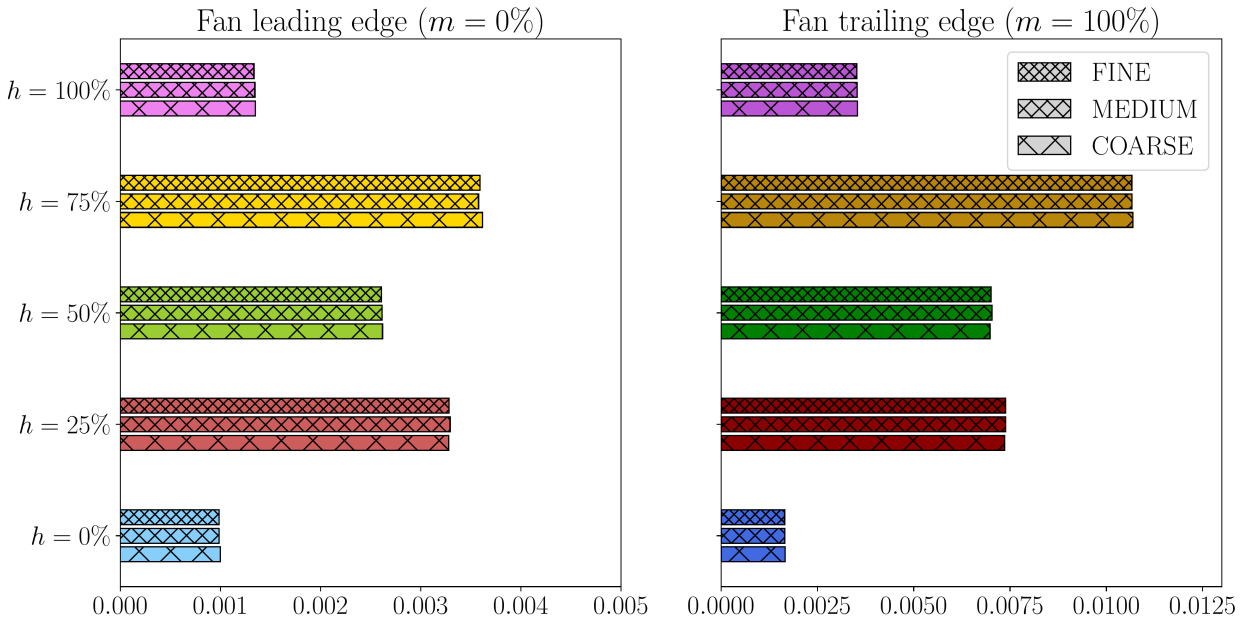

Fig. 9 Mesh convergence of the BFM gradients

V. Assessment of the ABFM capability to perform compressor shape design

A. ABFM design capability assessment methodology

This Hall adjoint formulation allows us to precisely evaluate the ability of the ABFM to conduct compressor shape optimization under clean inflow conditions, and to perform a first assessment of its capabilities under inlet distortions. In the context of simultaneous coupled optimizations of both the airframe and the engine geometries for aircraft configurations featuring a strong aerodynamics coupling between those subsystems, the gradients of the engine performance metrics with respect to the blade shape parameters must have the same sign and amplitude as their bladed counterpart over a large portion of the engine characteristic. In fact, under azimuthal inlet distortions, such as the BLI distortion of an engine embedded into the airframe, a given blade-to-blade channel experiences different operating conditions during its revolution. As a consequence, it describes an orbit on the engine characteristics, as observed by Godard in [6] for instance. Therefore, the body-force sensitivities must be relevant for all these operating conditions to be usable for preliminary fan design under azimuthal inlet distortions. If they prove relevant for several operating points of the engine characteristic, the ABFM would very likely prove to be an efficient tool to conduct fan shape optimization under inlet distortions.

Indeed, if a body-force simulation models $N_{sectors}$ of a blade row under azimuthal inlet distortions, it can be interpreted as $N_{sectors}$ single blade-to-blade channels, with different clean inflow conditions in each one of them. Indeed, the Hall model [5] rely on an axisymmetry hypothesis of the row inlet flow conditions over each blade-to-blade passage, in which the modeled blade force is uniformly smeared-out along the azimuthal direction. Therefore, provided the distortion characteristic length is greater than the larger of a blade-to-blade channel, the blade shape gradients of the full body-force simulation - i.e. with the $N_{sectors}$ sectors simulated - can therefore be approximated, at first, as the mean of the sensitivities evaluated on each one of the $N_{sectors}$ channels individually. Therefore, if one knows that the ABFM correctly predicts the fan shape gradients for each of these clean inflow conditions, then it is expected to correctly assess the fan shape gradients of the $N_{sectors}$ configuration under azimuthal inlet distortions. Once the ABFM accuracy has been established on a large part of the engine characteristic, one must then conduct a fan shape optimization under azimuthal inlet distortion and evaluate the ABFM-optimal configuration performance using unsteady RANS simulation to validate this assumption.

Considering now a purely radial inlet distortion, the constraints on the ABFM predictions are lower. If the ABFM can accurately predicts the fan shape gradients at flow adaptation, and their correct sign and amplitude at off-design conditions, then the ABFM-driven optimizations would most probably reach an optimal geometry very close to its blade-resolved counterpart, since it can reach fan adaptation at each radial position in each channel sector. This assumption can then be further confirmed before performing a fan shape optimization, by comparing ABFM and blade-resolved gradients under radial inlet distortions, since the stationnary-adjoint solver is still suitable for the latter.

To propose a first assessment of the ABFM design capabilities for compressors, we select three operating points on the engine characteristic to compare in details the blade-resolved gradients to those obtained with both body-force models, for both the fan and the stator. In addition to the operating point previously selected in IV.E, denoted $\dot{m}_{ME}$ from now on, we select a point near the stability limit, i.e. near the onset of the $\left(\dot{m}, \Pi_{\text{stage}}\right)$ positive slop. We choose a point near $\dot{m}_{SL} \approx 10.5$ kg.s^{-1}, which correspond to a 111 300 Pa outlet static pressure on the blade-resolved simulations. We also select an operating point near the blockage at $\dot{m}_{BLO} \approx 13.5$ kg.s^{-1}, corresponding to a 96 400 Pa outlet static pressure on the blade-resolved simulations. At first, we use the same fan parametrization used in IV.C. For the blade-resolved simulations, primal computations were undertaken with a uniform static outlet pressure P_{OUT}, and gradients were evaluated with the 'legacy' *elsA* adjoint-parameter method, as opposed to its modernized module. To compare those to the body-force gradients, the engine operating point must be the same. To do so, we perform the comparison by enforcing the same outlet mass flow rate across the BFM mesh than its blade-resolved counterpart. The procedure was described in IV.C and consists of a first BFM computation with a radial equilibrium, to find the static pressure map associated to the desired $\dot{m}_{OUT}$, and then a second computation using this static pressure map as the outlet boundary condition. The adjoint system is then solved using this CFD solution, and the gradients are evaluated with the adjoint-parameter method, using once again a $0.1°$ absolute step on the camber parameters. First, a comparison of both $\dot{m}$ and the compressor power consumption for this stage between the blade-resolved and the body-force simulations are undertaken in Table 3. For the bladed simulations, the power consumption is evaluated with the dedicated in-house ONERA's software, while for the body-force simulations it is evaluated using the Q_{POW} function implemented in *BACARDI*.

Mass flow rates crossing the body-force equivalent full-annulus configuration compare very well to their blade-resolved counterpart, with relative differences of about -0.01% for all selected operated conditions, as expected. It is

Operating point	Stability limit		Near design conditions		Near blockage	
	$\dot{m}_{OUT}$ (kg.s^{-1})	Power (W)	$\dot{m}_{OUT}$ (kg.s^{-1})	Power (W)	$\dot{m}_{OUT}$ (kg.s^{-1})	Power (W)
BFM	10.5231	$1.446\,10^5$	12.0769	$1.412\,10^5$	13.6115	$1.281\,10^5$
Bladed	10.5245	$1.422\,10^5$	12.0778	$1.376\,10^5$	13.6122	$1.127\,10^5$
difference (%)	*-0.013*	*1.70*	*-0.008*	*2.61*	*-0.005*	*13.7*

Table 3 Comparison of the outlet mass flow and the compressor power consumption between the blade-resolved and the body-force simulations, for the three chosen operating conditions.

therefore correct to compare the body-force gradients to their bladed counterparts, as they are evaluated for almost the same engine operating point. Similarly, the compressor power consumption compares well to the blade-resolved simulations, except near the blockage where a 13.7% difference arises. This overestimation of the compressor work near the metal blockage is consistent with the observations previously made on the engine characteristic, and may alter the gradient precision at this operating conditions.

B. Fan shape gradients comparison

Fan shape gradients comparison between the blade-resolved simulations and body-force simulations are respectively given in Figure 10a for the stability limit operating conditions, in Figure 10b for the point near maximum efficiency and in Figure 10c for the point near the blade metal blockage. The blade-resolved shape gradients were validated against centered finite-differences (not shown here), using an absolute step of 10^{-4} degrees, for the $\dot{m}_{ME}$ operating conditions. A maximum relative differences between the blade-resolved adjoint gradients and the finite-differences of 4.3% was observed, at the leading edge and $h = 25\%$ channel height. We observed that most of the relative differences are below 0.6% for the trailing edge control points, and below 2.3% at the leading edge.

We can observe in Figure 10b a very good match between the blade-resolved and the body-force gradients, for the $\dot{m}_{ME}$ operating point. The quadratic losses of the QNC model strongly enhanced the ABFM gradients evaluation, with most gradients within −3 to +5% of the blade-resolved evaluations for the QNC model, which performs the best. We can notice two control points, $\beta^{fan}_{h_0\,m_{100}}$ and $\beta^{fan}_{h_{100}\,m_0}$ as defined in Figure 7a, for which the ABFM-QNC gradient prediction is less accurate, with a respective relative difference to their blade-resolved counterpart of −27% and +14%. These differences can be explained by the presence of large tri-dimensional flow structures at these locations of the fan that cannot be captured by the BFM models. Indeed, at the fan trailing edge, near the hub, the corner vortex is well developed and the flow velocity is reduced. In such regions, it has been observed that the normal force of the Hall model underestimates the blade work [8], and therefore the gradient of the power delivered by the fan with respect to the skeleton camber in that region. It also explains why the QNC model does not perform better than the HNL model at the base of the fan trailing edge. At the fan leading edge, near the shroud, the body-force model does not capture the tip-leaking vortex that alter the flow incidence with respect to the blade. Both body-force models over-estimate the gradient of Q_{POW} in that region. However, the QNC model performs slightly better in that region than the HNL model, since it captures some of the high-incidence effects the fan perceives in the blade-resolved simulations. In Figure 10a, we observe that near the stability limit, the ABFM gradient evaluation is less accurate but remains very close to the blade-resolved ones. Once again, the QNC performs better than the HNL model, except at 25% of channel height. A better comparison of the QNC to the blade-resolved results was expected since this model allows to take into account some of the non-linear effects and losses induced by the misalignment between the skeleton and the flow for such operating conditions.

Finally, in Figure 10c, we observe notable differences between the ABFM and the blade-resolved gradients, mainly at the leading edge, with gradient relative differences between −18% and −66% for the QNC model. Contrary to the previous operating points, the QNC gives less accurate gradients than the HNL model, but both suffers from the same tendency errors. Indeed, they both fail to capture the strong increase of the gradients at the fan leading edge compared to the $\dot{m}_{ME}$ operating point, while their blade-resolved counterpart have been multiplied by a factor of 2 to 3 for channel heights between 25 and 75%. Radial views of the RANS simulation for this operating point, given in Figure 11 for $h \approx 25\%$ and $h \approx 75\%$ channel height, show a recirculation at the fan leading edge. At $h \approx 25\%$, a significant thickening of the boundary-layer is observed on the pressure side, while the boundary layer has separated at $h \approx 75\%$. This recirculation zone can be observed starting from the hub, and up to $r = 0.27$ m, almost at the blade tip. These phenomena appear to be responsible for the high gradient values on the fan leading edges. The blade-resolved

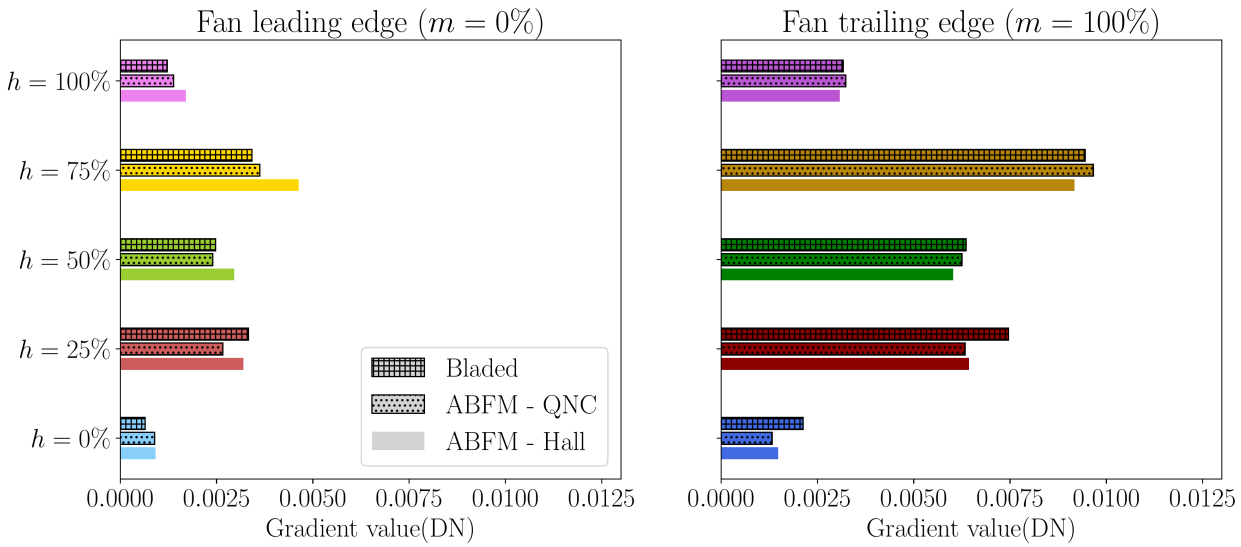

(a) Gradient comparison for operating conditions near the stability limit

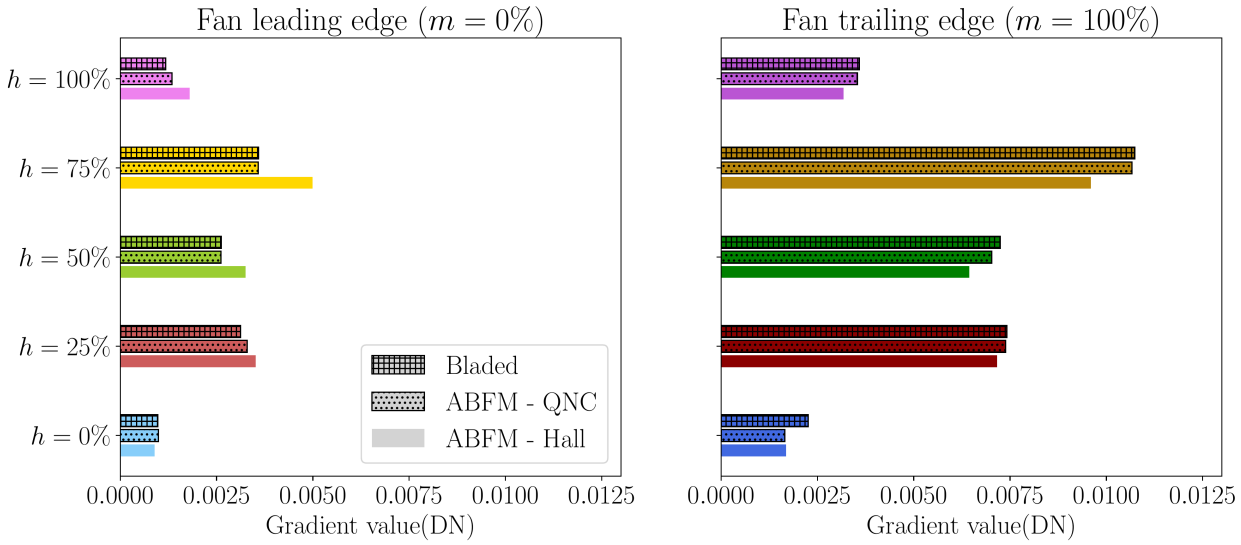

(b) Gradient comparison for operating conditions near max efficiency in the stable part of the engine characteristic

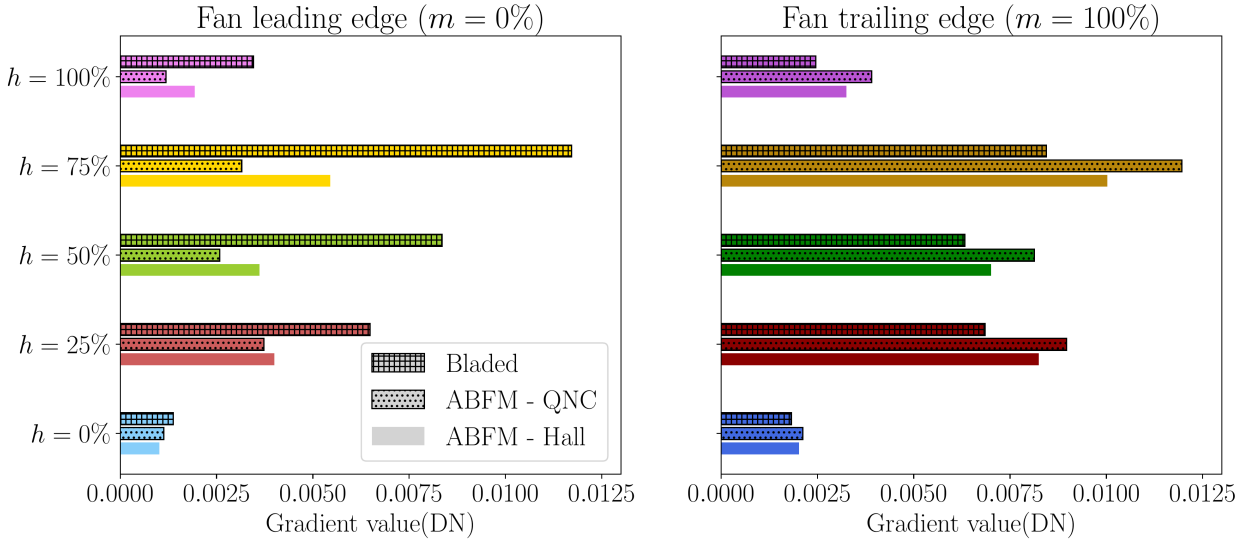

(c) Gradient comparison for operating conditions near the blockage

Fig. 10 Fan shape gradients comparison between blade-resolved adjoint-parameter evaluations and ABFM adjoint-parameter evaluations for the Q_{POW} function for $\dot{m} \approx 10.5$ kg.s^{-1} (a), 12 kg.s^{-1} (b) and 13.5 kg.s^{-1} (c).

gradient amplitude increases with the channel height, which may be explained by the increase of the recirculation zone length and of the pressure-side boundary-layer thickness, which ultimately separates. Indeed, as one can observe by comparing Figures 11a to 11b for the total pressure ratio and Figures 11c to 11d for the Mach contours, as the radius increases, the length of both the recirculation zone and of the low Mach number and low total pressure zone increases as well. For $h \approx 75\%$ channel height, the flow separation reaches the trailing edge. Since the Hall formulation relies on a thin-airfoil approximation, it cannot capture non-linear and local effect on the blade skin such as recirculation zones, flow separation and aerodynamic blockage due to boundary layer thickening. In addition, we can observe that Mach number locally reaches up to 0.85 near the fan leading edge, at the suction side. At such Mach numbers, compressibility effects may noticeably influence the blade work in those regions, and therefore their gradients. For the same reason as previously exposed, the Hall model cannot capture most of the compressibility effects. For instance, on body-force simulations at $\dot{m}_{BLO}$, the maximum Mach number observed on the fan block reaches up 0.4, near the hub. Those two fundamental limitations of the Hall model explain the strong underestimation of the gradients at the leading edge.

Since the BFM simulation cannot predict the boundary layer thickening nor the flow separations previously observed for this operating condition, the ABFM sensitivities over-estimate the blade work that can be gained by increasing the fan camber at the trailing edge, which explain the differences observed between the ABFM gradients and their blade-resolved counterpart on the right part of Figure 10c. Gradient relative differences between 17 and 59% of the blade-resolved gradient value are observed for the QNC model.

Enhancing the ABFM gradient predictions for this operating point will therefore require to capture at least some of the non-linear effects induced by the fan boundary layers at off-design operating conditions. If analytical models have been introduced to increase the BFM models fidelity at the metal blockage [4, 8, 29] and compressibility corrections have been added by Thollet [8] to account for some of the compressibility effects on the blade work, they cannot model the non-linear local flow phenomena at off-design operating conditions. Therefore, no analytical model can yet predict the boundary-layer influence on the blade work and on the entropy generation without pre-requisite calibration. The artificial intelligence may be of help in that matter, as attempted by Pazireh [30] in 2021. He trained a neural network to predict the boundary layer thickness, and used this data in an analytical model that predicts the associated entropy generation. If this new parallel force has proven capable to improve the predictions at off-design condition, and even at transonic conditions, it however requires an important database to train the model. Besides, the model prediction was not guaranteed at all operating conditions. Nevertheless, it can be a way to improve the gradient predictions, taking into account more precisely viscous effects and aerodynamic blockage into account.

Despite some limitations, the results presented in Figure 10 are very encouraging, since they show that the body-force gradients stay relevant on a large part of the engine characteristic. Using such gradients for fan shape optimization, even under inlet distortions, should drive the fan design in the correct direction, and may prove to be a very efficient pre-design tool, especially when dealing with radial inlet distortions. Without additional model taking into account some of the compressibility effects, like the metal blockage, these pre-design capabilities are expected to be reduced for transonic fan optimizations under azimuthal distortions.

One can finally wonder if the ABFM still performs well with a finer parametrization of the fan skeleton, meaning if the ABFM is capable to correctly capture very local sensitivities. To assess this capacity, we perform an evaluation of 55 camber gradients on the blade skeleton, comparing them to their blade-resolved counterparts. Gradients are evaluated at 0, 10, 20, 30, 40, 50, 60, 70, 80, 90 and 100% of the channel height, and at 0, 25, 50, 75 and 100% of the fan chord. We perform this comparison for the same three operating points previously studied. Results are given respectively in Figure 12a for $\dot{m}_{ME}$ and in Figure 12b for $\dot{m}_{BLO}$. For $\dot{m}_{SL}$, results are not shown since they are very similar to the ones obtained for the $\dot{m}_{ME}$ operating point.

The adjoint formulation of the QNC model reproduces very well the local camber sensitivities for the $\dot{m}_{SL}$ and $\dot{m}_{ME}$ operating conditions. Small discrepancies can be observed at $h = 10\%$ of the channel height, between the leading edge and 50% of the local fan chord, in Figure 12a. In that region, the ABFM underestimates the gradients. Local errors can also be observed on the leading edge, between 70 and 90% of the channel height, where once again the ABFM underestimates the gradients compared to their bladed counterpart. Elsewhere, both the spatial distribution and the gradient values are very well reproduced. The gradient of maximum amplitude is correctly estimated, both in terms of its position, at 90% of the channel height and 75% of the chord, as well as in terms of its dimensionless value of 0.0035. Near the blockage, where gradients discrepancies were previously observed with the limited set of camber parameters, we can clearly confirm that the QNC model cannot capture the strong variations of the gradient distribution. In the left part of Figure 12b, we can observe an ABFM gradient map very similar to the one observed at $\dot{m}_{ME}$, with gradients of higher amplitude. On the contrary, the blade-resolved gradients map shows a very different behaviour. The strong gradients observed along the line of 75% relative chord is greatly attenuated, while high positive gradients are observed

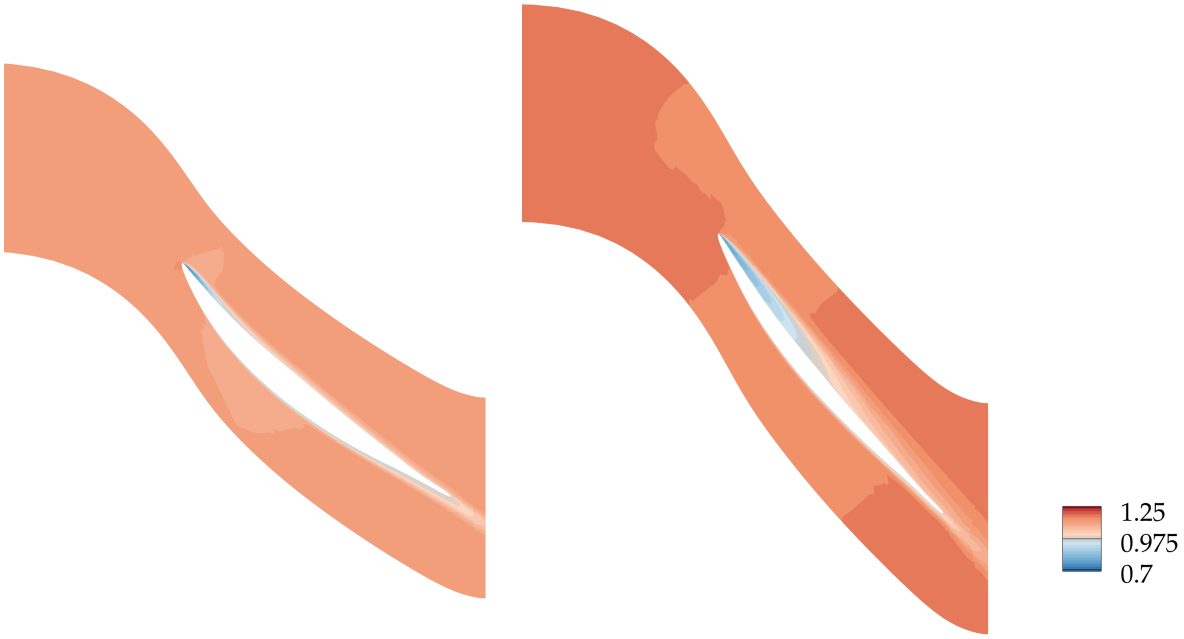

(a) Radial cut of total pressure ratio contours at $r = 0.225$ m

(b) Radial cut of total pressure ratio contours at $r = 0.259$ m

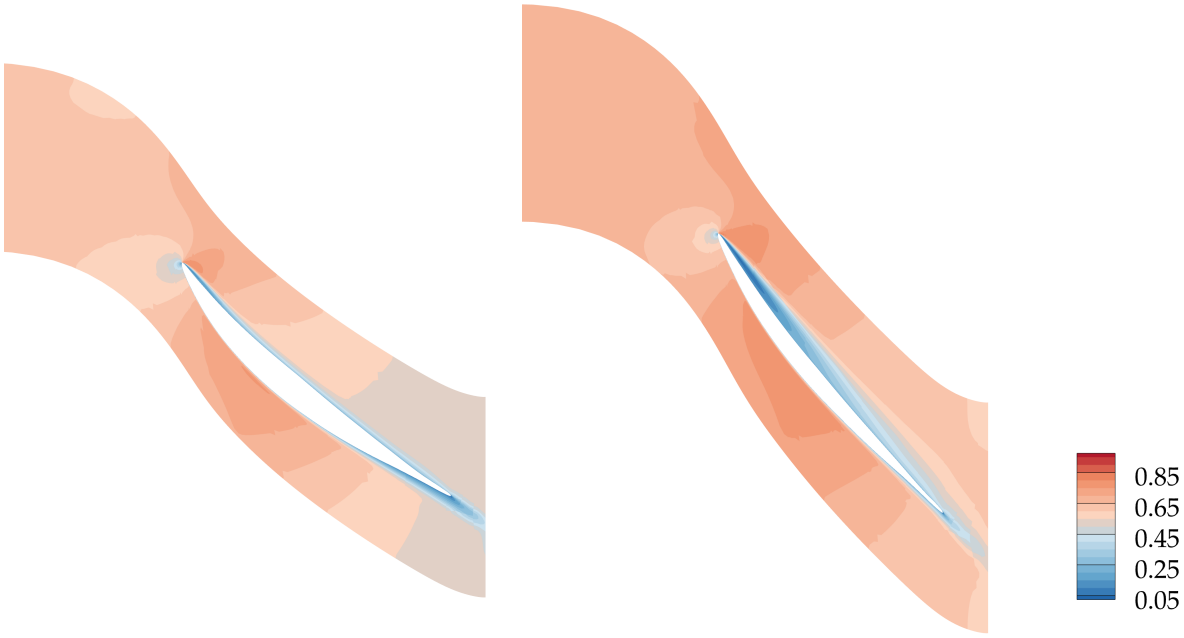

(c) Radial cut of Mach contours at $r = 0.225$ m

(d) Radial cut of Mach contours at $r = 0.259$ m

Fig. 11 Up: Total pressure ratio contours. Down: Mach number contours. Radial cuts on the fan blade near $h \approx 25\%$ (left) and $h \approx 75\%$ (right) of the channel height at $\dot{m} \approx 13.5$ kg.s^{-1}.

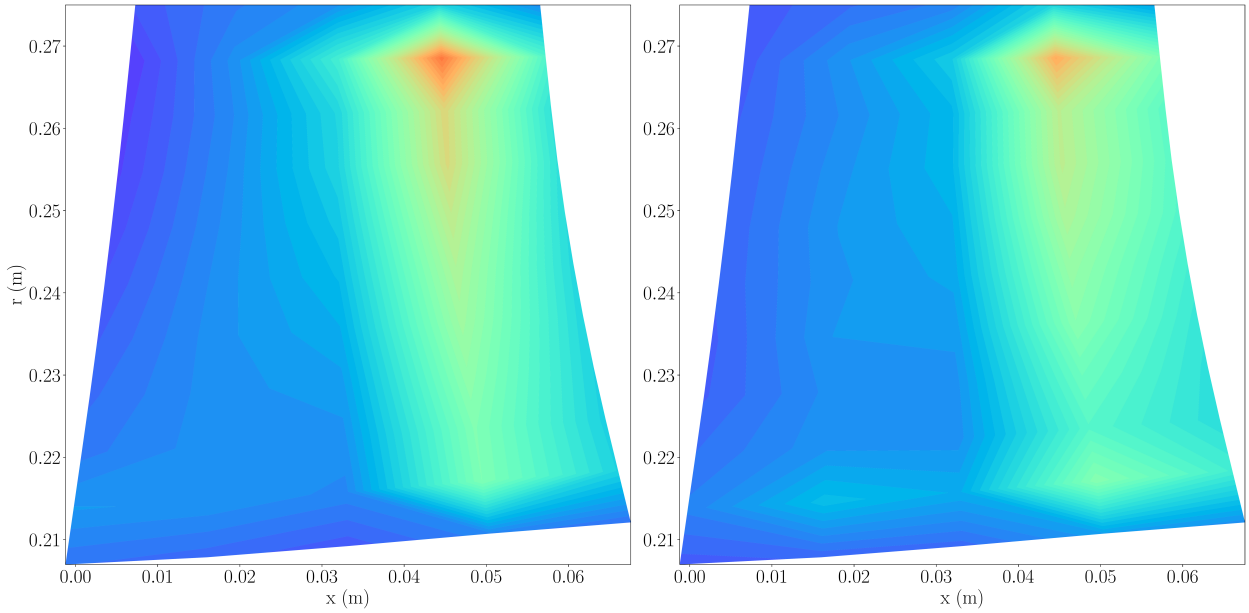

(a) Camber gradients map at $\dot{m} \approx 12$ kg.s^{-1}

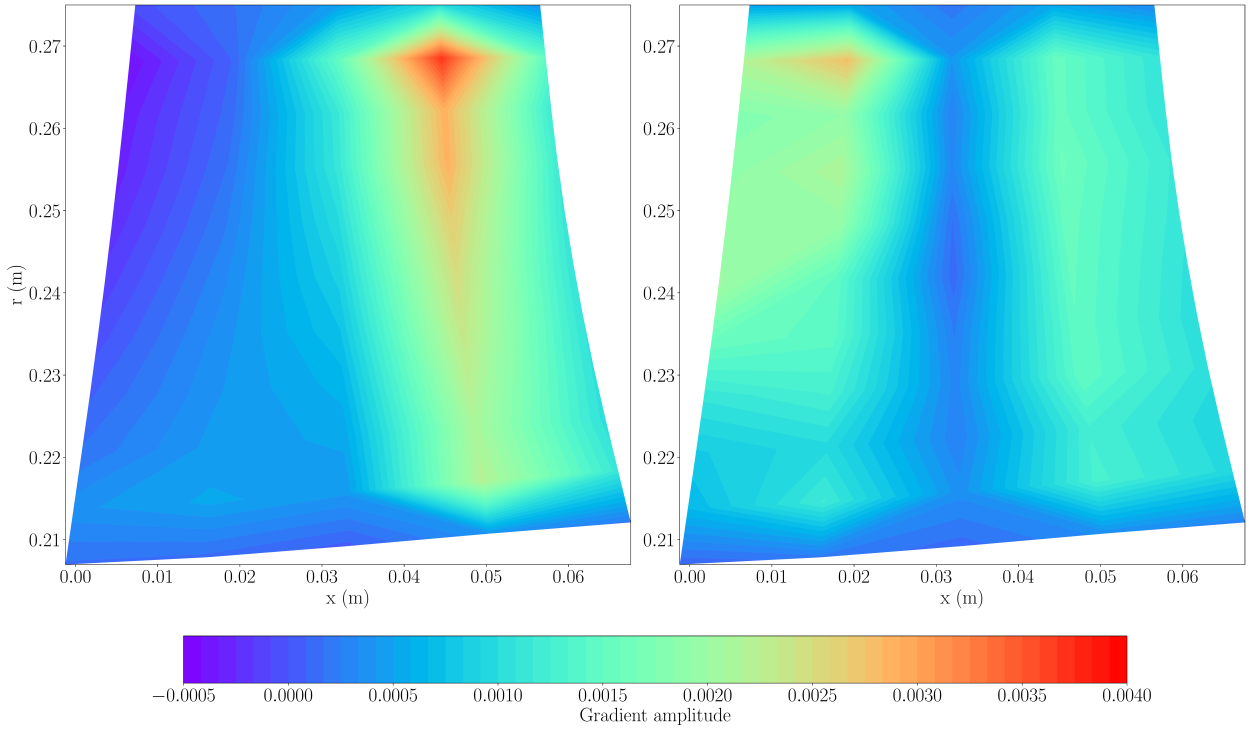

(b) Camber gradients map at $\dot{m} \approx 13.5$ kg.s^{-1}

Fig. 12 Meridional map of Q_{POW} camber gradient evaluations on the fan skeleton for the refined parametrization, evaluated with the QNC body-force model (left) and with blade-resolved simulations (right), near design operating conditions (up) and near blockage (down).

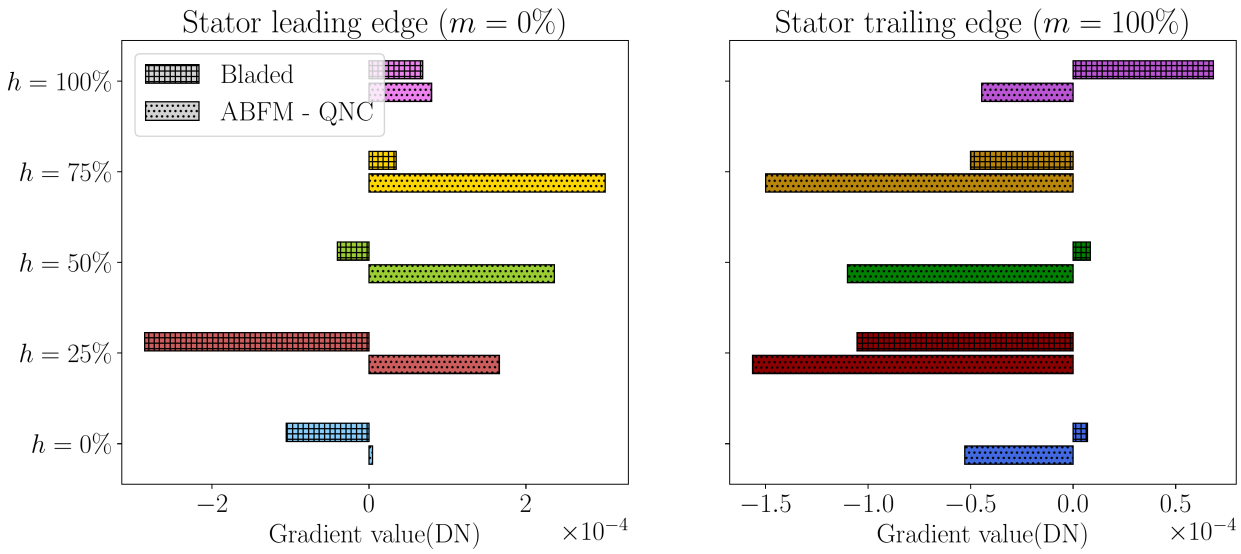

Fig. 13 Stator shape gradients comparison between blade-resolved adjoint-parameter evaluations and ABFM adjoint-parameter evaluations for the Q_{POW} function for $\dot{m} \approx 12$ kg.s^{-1}.

near the leading edge, especially above 50% of the channel height. Finally, camber gradients are drastically reduced in the middle of the blade, along the line of 50% relative chord.

Therefore, the adjoint body-force can provide very precise gradients in the stable part of the engine characteristics, even close to the stability limit. Even with a very fine parametrization of the fan skeleton, gradients are very well reproduced for these operating conditions. However, near the blockage, a limited set of parameters seems more appropriated without further modeling improvements.

C. Stator shape design

Since we have assessed some of the ABFM capabilities for fan design optimizations, we now undertake the same evaluation for the stator. We still consider the Q_{POW} function, even if the stator does not directly contribute to the power transmitted to the fluid. Through upstream potential effects, it can redistribute the flow around the fan and therefore affect, at lower orders of magnitude than the fan itself, the total power consumption. Considering the first set of 10 camber parameters defined in section IV.C, we evaluate the ABFM gradients for the QNC model and their blade-resolved counterpart. Considering the results obtained so far, we present only those for the most favourable operating condition $\dot{m}_{ME}$ in Figure 13. One can first observe that the gradients with respect to the camber control points are two order of magnitudes lower for the stator, than those previously measured for the rotor (see Figure 10). These very small gradients are more strongly affected by the body-force approximations, and its limitations in capturing non-linear flow features. Besides, in a body-force simulation, the stator incoming flow suffers from the model inaccuracies made on the rotor simulation. Therefore, it is coherent to observe a poor gradient prediction on the stator for the Q_{POW} objective function. Several body-force gradients do not have the right sign - for h = 0, 25, 50% at the leading edge and h = 0, 50 and 100% at the trailing edge - and most of them do not have the correct amplitude. An attempt was made to compare the ABFM gradients to their blade-resolved counterpart for pitch control points along the channel height, but the obtained gradients were still inaccurate.

However, in the scope of fan-stator optimization, the main role of the stator lies in its contribution to the thrust and to the compression ratio, through the conversion of the fan-induced swirl into static pressure rise. Since it has been observed that the body-force reproduces very well the swirl conversion into static pressure across the stator row, one can expect that stator shape gradients for the thrust - as the investigated QoI - would be better predicted by the ABFM. If their amplitude proves to be, as expected, several orders of magnitude higher those measured for Q_{POW} on the stator, the shape optimization driven by ABFM sensitivities would still go in the right direction.

VI. Conclusions and ways forward

In this study, the normal force of the Hall model has been implemented and validated in the in-house library *BACARDI*. The Hall model has been enriched using the parallel force described in eq. (11), without any calibration data in its formulation. Then, using the algorithmic differentiation tool Tapenade [24], the adjoint formulation of the normal force and of the non-calibrated parallel force has been implemented. Then, both have been validated using finite-differences gradient checks. A mesh convergence study on the body-force simulation has shown almost no influence of the mesh refinement on the compressor performance metrics, nor on the power consumption gradients.

Next, a comparison between adjoint body-force gradients and their blade-resolved counterpart has been undertaken, for three operating conditions chosen in key points of the compressor characteristic. It has been observed that the adjoint body-force formulation of the Hall model with not calibrated quadratic losses can provide very precise gradients in the stable part of the engine characteristics, even close to the stability limit. Even with a very fine parametrization of the fan skeleton, the spatial distribution of the shape gradients is very well reproduced for these operating conditions. However, near the blockage, the body-force model cannot capture crucial flow features on the fan. Nevertheless, with a limited set of parameters, it can still assess rather correctly the gradient sign and amplitude.

These first results encourage the use this new ABFM tool to perform fan shape design, even under radial distortions and when using a detailed parametrization of the fan, at a far lower cost than classical methods. This must be confirmed by a comparison between ABFM and blade-resolved gradients under radial inlet distortions, which is the subject of ongoing investigations. Under azimuthal distortions, if the fan enters the blockage region during its revolution, the current ABFM design capabilities might be reduced. Using a limited set of parameters, it might still provide the correct descent direction to an optimizer, but cannot yet be used for a detailed shape optimization of the fan without further modeling improvements. To overcome these limitations, it appears necessary to improve the body-force model predictions at off-design conditions. Some tools are already available in the literature, mainly to extend the ABFM design capabilities to transonic compressors. However, they are not suited to the aerodynamic blockage modelization issue encountered in this particular test case. For the stator, the gradients of the compressor power consumption with respect to the camber control points are strongly mispredicted.

Before concluding on the current ABFM capability to conduct fan and stator shape optimization, even under inlet distortions, the present study must be extended to other quantities of interest, such as the compressor generated thrust and pressure compression ratio, and also to other blade shape parameters, like chord deformations. Then, this new tool could be integrated in a turbofan secondary airflow shape optimization, and eventually in an aero-propulsive coupled optimization. In this last case, one could first assess the contribution of the Hall model to the airframe shape gradients. Then, in a second time, a simultaneous optimization of both the airframe and the compressor shapes may be undertaken.

VII. Acknowledgments

The authors would like to thank Dr. Antoine Dumont who provided the tool enabling us to perform the blade-resolved analysis and gradient evaluations, and who shared his valuable expertise on these topics. The authors would also like to thank Dr. Antoine Riols-Fonclare for providing the mesh deformation tool used in the body-force mesh deformation and for his valuable assistance in implementing it in the present study.

This work was partially founded by the Clean Sky 2 Joint Undertaking project, granted by the European Union under grant agreement No CS2-LPA-GAM-2020-2021-01.

This study is also supported by the European project NEXTAIR which has received funding from the European Union's Horizon Europe research and innovation program under grant agreement No 101056732. Views and opinions expressed are however those of the authors only and do not necessarily reflect those of the European Union. Neither the European Union nor the granting authority can be held responsible for them.

References

[1] Delbecq, S., Fontane, J., Gourdain, N., Mugnier, H., Planès, T., and Simatos, F., "Aviation and Climate : a literature review," Tech. Rep. 1.1, ISAE-SUPAERO, Toulouse, France, 2022.

[2] Association, I. A. T., "Working Towards Ambitious Targets," , 2021. URL https://www.iata.org/en/programs/environment/climate-change/.

[3] Peters, A., Spakovszky, Z. S., Rose, B., and Lord, W. K., "Ultra-Short Nacelles for Low Fan Pressure Ratio Propulsors," *American Society of Mechanical Engineers*, 2014, p. 15.

[4] Godard, B., "Étude et méthodologies de simulation de doublet entrée d'air - soufflante pour la conception de turbofan de nouvelle génération," PhD Thesis, Université de Toulouse, 2018.

[5] Hall, D. K., "Analysis of civil aircraft propulsors with boundary layer ingestion," PhD Thesis, MIT, 2015. URL http://hdl.handle.net/1721.1/97353.

[6] Godard, B., De Jaeghere, E., and Gourdain, N., "Efficient Design Investigation of a Turbofan in Distorted Inlet Conditions," *Volume 2A: Turbomachinery*, American Society of Mechanical Engineers, Phoenix, Arizona, USA, 2019, p. V02AT39A011. https://doi.org/10.1115/GT2019-90471, URL https://asmedigitalcollection.asme.org/GT/proceedings/GT2019/58554/Phoenix,%20Arizona,%20USA/1066452.

[7] de Vega, L. L., Guillaume, D., and Nicolas, G. R., "Fully Coupled Body Force–Engine Performance Methodology for Boundary Layer Ingestion," *Journal of Propulsion and Power*, Vol. 37, No. 2, 2021. https://doi.org/https://doi.org/10.2514/1.B37743.

[8] Thollet, W., "Modélisations simplifiées de turbomachines pour l'analyse par la simulation des installations motrices complexes d'avions/Body force modeling of fan-airframe interactions," PhD Thesis, Université de Toulouse, Jul. 2017.

[9] Ordaz, I., Rallabhandi, S. K., Nielsen, E. J., and Diskin, B., "Mitigation of Engine Inlet Distortion through Adjoint-Based Design," *35th AIAA Applied Aerodynamics Conference*, American Institute of Aeronautics and Astronautics, Denver, Colorado, 2017. https://doi.org/10.2514/6.2017-3410, URL https://arc.aiaa.org/doi/10.2514/6.2017-3410.

[10] Kenway, G. K., and Kiris, C. C., "Aerodynamic Shape Optimization of the STARC-ABL Concept for Minimal Inlet Distortion," *2018 AIAA/ASCE/AHS/ASC Structures, Structural Dynamics, and Materials Conference*, American Institute of Aeronautics and Astronautics, Kissimmee, Florida, 2018. https://doi.org/10.2514/6.2018-1912, URL https://arc.aiaa.org/doi/10.2514/6.2018-1912.

[11] Gray, J. S., and Martins, J. R. R. A., "Coupled aeropropulsive design optimisation of a boundary-layer ingestion propulsor," *The Aeronautical Journal*, Vol. 123, No. 1259, 2019, pp. 121–137. https://doi.org/10.1017/aer.2018.120, URL https://www.cambridge.org/core/product/identifier/S0001924018001203/type/journal_article.

[12] Ordaz, I., Nielsen, E. J., and Wang, L., "Design of a Distributed Propulsion Concept Using an Adjoint-Based Approach and Blade Element Theory to Minimize Power," *AIAA AVIATION 2020 FORUM*, American Institute of Aeronautics and Astronautics, VIRTUAL EVENT, 2020. https://doi.org/10.2514/6.2020-2632, URL https://arc.aiaa.org/doi/10.2514/6.2020-2632.

[13] Carnevale, M., Wang, F., Green, J. S., and Mare, L. D., "Lip Stall Suppression in Powered Intakes," *Journal of Propulsion and Power*, Vol. 32, No. 1, 2016, pp. 161–170. https://doi.org/10.2514/1.B35811, URL https://arc.aiaa.org/doi/10.2514/1.B35811.

[14] Gray, J. S., Mader, C. A., Kenway, G. K. W., and Martins, J. R. R. A., "Coupled Aeropropulsive Optimization of a Three-Dimensional Boundary-Layer Ingestion Propulsor Considering Inlet Distortion," *Journal of Aircraft*, Vol. 57, No. 6, 2020, pp. 1014–1025. https://doi.org/10.2514/1.C035845, URL https://arc.aiaa.org/doi/10.2514/1.C035845.

[15] Yildirim, A., Gray, J. S., Mader, C. A., and Martins, J. R. R. A., "Coupled Aeropropulsive Design Optimization of a Podded Electric Propulsor," *AIAA AVIATION 2021 FORUM*, AIAA AVIATION FORUM, VIRTUAL EVENT, 2021. https://doi.org/10.2514/6.2021-3032.

[16] Lamkin, A., Yildirim, A., Martins, J. R. R. A., and Wukie, N. A., "Advancements in Coupled Aeropropulsive Design Optimization for High-Bypass Turbofan Engines," *AIAA AVIATION 2023 FORUM*, AIAA AVIATION FORUM, San Diego, California, 2023. https://doi.org/10.2514/6.2023-3591.

[17] Godard, B., Ben Nasr, N., Barrier, R., Marty, J., Gourdain, N., and De Jaeghere, E., "Methodologies for Turbofan Inlet Aerodynamics Prediction," *35th AIAA Applied Aerodynamics Conference*, American Institute of Aeronautics and Astronautics, Denver, Colorado, 2017. https://doi.org/10.2514/6.2017-3413, URL https://arc.aiaa.org/doi/10.2514/6.2017-3413.

[18] Thollet, W., Dufour, G., Carbonneau, X., and Blanc, F., "Assessment of Body Force Methodologies for the Analysis of Intake–Fan Aerodynamic Interactions," *American Society of Mechanical Engineers*, 2016, p. 9.

[19] Kiffer, T., Dufour, G., Gojon, R., Thollet, W., and de Vega, L. L., "Extension and validation of the Body Force Method to a propeller blade," *AIAA AVIATION 2023 FORUM*, San Diego, California, 2023. https://doi.org/10.2514/6.2023-3378.

[20] Latour, M. T., "Body force modeling of axial turbomachinery for analysis and design optimization," Tech. rep., TU Delft, Apr. 2020. URL https://repository.tudelft.nl/islandora/object/uuid%3A03309dd3-0fe7-4c4d-acb7-db1371e3d945.

[21] Morvillo, G., "Application of body force modeling to aeroengine fan blade design," Tech. rep., TU Delft, 2021. URL https://www.politesi.polimi.it/retrieve/9c33cfa7-c56d-4ce2-a8fc-8dfcf960a02f/Gabriele_Morvillo_Tesi.pdf.

[22] Cambier, L., Heib, S., and Plot, S., "The Onera elsA CFD software: input from research and feedback from industry," *Mechanics & Industry*, Vol. 14, No. 3, 2013, pp. 159–174. https://doi.org/10.1051/meca/2013056, URL http://www.mechanics-industry.org/10.1051/meca/2013056.

[23] Peter, J., Renac, F., Dumont, A., and Méheut, M., "Discrete Adjoint Method for Shape Optimization and Mesh Adaptation in the elsA Code. Status and Challenges," *50h 3AF International Conference on Applied Aerodynamics*, Toulouse, France, 2015, p. 14.

[24] Hascoet, L., and Pascual, V., "The Tapenade automatic differentiation tool: Principles, model, and specification," *ACM Transactions on Mathematical Software*, Vol. 39, No. 3, 2013, pp. 1–43. https://doi.org/10.1145/2450153.2450158, URL https://dl.acm.org/doi/10.1145/2450153.2450158.

[25] Dosne, C., Barrier, R., Bourasseau, S., Carini, M., Moretti, R., and Peter, J., "An Adjoint Body-Force Approach for Fully-Coupled Aero-Propulsive Optimizations," Chania, Greece, 2023. URL https://hal.science/hal-04146020.

[26] Maugars, B., Bourasseau, S., Content, C., Michel, B., Berthoul, B., Ramirez, J. N., Raud, P., and Hascoët, L., "Algorithmic Differentiation for an efficient CFD solver," *ECCOMAS 2022 - 8th European Congress on Computational Methods in Applied Sciences and Engineering*, Oslo, Norway, 2022, p. 22. https://doi.org/hal-03759125.

[27] Peter, J., "Contributions to discrete adjoint method in aerodynamics for shape optimization and goal-oriented mesh adaptation," HDR Thesis, Université de Nantes, Sep. 2020.

[28] Carrier, G., Destarac, D., Dumont, A., Meheut, M., Salah El Din, I., Peter, J., Ben Khelil, S., Brezillon, J., and Pestana, M., "Gradient-Based Aerodynamic Optimization with the elsA Software," *52nd Aerospace Sciences Meeting*, American Institute of Aeronautics and Astronautics, National Harbor, Maryland, 2014. https://doi.org/10.2514/6.2014-0568, URL http://arc.aiaa.org/doi/10.2514/6.2014-0568.

[29] Kottapalli, A. P., "Development of a Body Force Model for Centrifugal Compressors," Master's thesis, Massachusetts Institute of Technology, Aug. 2013.

[30] Pazireh, S., "Body Force Modeling of Axial Turbomachines Without Calibration," PhD Thesis, University of Windsor, Ontario, Canada, Mar. 2021.